Stability analysis of periodic solutions computed for blade-tip/casing contact problems

Yann Colaïtis, Alain Batailly

▶ **To cite this version:**

Yann Colaïtis, Alain Batailly. Stability analysis of periodic solutions computed for blade-tip/casing contact problems. Journal of Sound and Vibration, 2022, 538, pp.117219. 10.1016/j.jsv.2022.117219 . hal-03764770

HAL Id: hal-03764770
https://hal.science/hal-03764770v1

Submitted on 30 Aug 2022

HAL is a multi-disciplinary open access archive for the deposit and dissemination of scientific research documents, whether they are published or not. The documents may come from teaching and research institutions in France or abroad, or from public or private research centers.

L'archive ouverte pluridisciplinaire **HAL**, est destinée au dépôt et à la diffusion de documents scientifiques de niveau recherche, publiés ou non, émanant des établissements d'enseignement et de recherche français ou étrangers, des laboratoires publics ou privés.

POLYTECHNIQUE MONTRÉAL
UNIVERSITÉ D'INGÉNIERIE

LABORATOIRE D'ANALYSE VIBRATOIRE ET ACOUSTIQUE

Stability analysis of periodic solutions computed for blade-tip/casing contact problems

Y. Colaïtis[1], A. Batailly[1]

Abstract

This article focuses on the stability assessment of mechanical systems featuring a nonlinear interface on which are applied unilateral contact constraints. The regularized-Lanczos harmonic balance method is used to compute periodic solutions for each system. For each considered mechanical system, the implementation of distinct stability assessment numerical algorithms (including the Newmark $2n$-pass method and Hill's method using eigenvalue sorting) relying on Floquet theory allows for an in-depth investigation of their convergence and accuracy. From a single-degree of freedom impactor impacting a fixed obstacle to the industrial finite element model of a transonic compressor blade impacting a deformed casing, the gradually increasing complexity of the considered mechanical systems provides new insight on which stability assessment numerical algorithm may be the best suited when dealing with contact nonlinearities. From a numerical standpoint, attention is paid to specific developments that were identified as key for enhancing the numerical efficiency of the stability assessment process including the iterative solver, the computation of analytical derivatives, the scaling of the problem and the use of fast Fourier transforms. Particular attention is also paid to the influence of the Lanczos filtering procedure and its implications in terms of stability assessment. While it is found that both the Newmark $2n$-pass method and Hill's method with eigenvalue sorting can be successfully applied on large industrial systems featuring a nonlinear interface, the faster convergence of Hill's method is underlined and suggests it may be a better option for an accurate and efficient stability assessment on which Lanczos filtering has a negligible influence.

Keywords

harmonic balance method; numerical continuation; blade-tip/casing contacts; Floquet Theory; Hill's method; Newmark $2n$-pass method; rotor/stator interaction

1 - Department of Mechanical Engineering, École Polytechnique de Montréal, P.O. Box 6079, Succ. Centre-Ville, Montréal, Québec, Canada H3C 3A7

Analyse de stabilité des solutions périodiques calculées pour des problèmes de contact aube/carter

Y. Colaïtis[1], A. Batailly[1]

Résumé

Cet article se concentre sur l'évaluation de la stabilité de systèmes mécaniques comportant une interface non-linéaire sur laquelle est appliquée des contraintes de contact unilatéral. La méthode de l'équilibrage harmonique régularisée-filtrée est utilisée pour calculer les solutions périodiques de chaque système. Pour chaque système mécanique considéré, la mise en œuvre d'algorithmes numériques distincts d'évaluation de la stabilité (notamment la méthode de Newmark $2n$-passes et la méthode de Hill couplée à un tri des valeurs propres) reposant sur la théorie de Floquet permet une étude approfondie de leur convergence et de leur précision. D'un impacteur à un seul degré de liberté impactant un obstacle fixe au modèle éléments finis d'une aube industrielle de compresseur transsonique impactant la surface interne d'un carter, la complexité croissante des systèmes mécaniques considérés offre une nouvelle perspective sur le comportement numérique de l'algorithme d'évaluation de la stabilité pouvant être le mieux adapté pour traiter les non-linéarités de contact. D'un point de vue numérique, l'attention est spécifiquement portée sur des développements ayant été identifiés comme essentiels pour améliorer l'efficacité numérique du processus d'évaluation de la stabilité, notamment le solveur itératif, le calcul semi-analytique des dérivées, la mise à l'échelle du problème, et l'utilisation de transformées de Fourier rapides. Une attention particulière est également accordée à l'influence de la procédure de filtrage de Lanczos et à ses implications en termes d'évaluation de la stabilité. Bien que la méthode de Newmark $2n$-passes et la méthode de Hill couplée à un tri des valeurs propres puissent être appliquées avec succès sur des systèmes industriels de grande dimension comportant une interface non-linéaire, la convergence plus rapide de la méthode de Hill est soulignée et suggère qu'elle pourrait être une meilleure option pour une évaluation précise et efficace de la stabilité sur laquelle le filtrage de Lanczos a une influence négligeable.

Mots-clés

méthode de l'équilibrage harmonique; continuation numérique; contacts aube/carter; théorie de Floquet; méthode de Hill; méthode Newmark $2n$-passes, interaction rotor/stator

1 - Département de génie mécanique, École Polytechnique de Montréal, P.O. Box 6079, Succ. Centre-Ville, Montréal, Québec, Canada H3C 3A7

1 Introduction

The prediction of the vibration response of nonlinear mechanical systems has long been investigated by researchers. In the aerospace industry in particular, characterizing the dynamics of structural components featuring nonlinear interfaces related to friction [1] or structural contacts [2] has been the focal point of many recent studies. Putting aside interactions related to aerodynamic phenomena, one may distinguish four key nonlinear interfaces within aircraft engines, namely the (1) shaft/bearing [3, 2], (2) blade/blade [4, 5], (3) disk/blade [6, 7, 1] and (4) blade-tip/casing interfaces [2, 8]. For some of these interfaces, due to the lack of suitable methodologies to predict and model sophisticated dynamic responses, typical design guidelines aim at preventing the occurrence of nonlinear structural interactions, be it at the expense of lowering the engine overall efficiency. However, the push towards reducing the environmental footprint of aircraft engines has shifted this paradigm and engineers must now account for nonlinear structural interactions in the early design stages of an aircraft engine. For aircraft engine blades, this means that design guidelines must evolve to account for intricate nonlinear vibration responses and possible shift of eigenfrequencies for instance. In a context where several experimental setups [9, 10, 11, 12, 13] underlined the detrimental consequences of nonlinear structural interactions on a blade's lifespan, designers need new tools and methodologies dedicated to the characterization of such sophisticated nonlinear interactions.

So far, each of the four aforementioned nonlinear interfaces have been investigated separately, using specific models and methodologies. With respect to the shaft/bearing interface for instance, simplified or analytical models featuring orbital motions around the axis of rotation have been widely used [14, 15, 16]. Numerical developments motivated by the understanding of rubbing phenomena at this interface drove the development efficient solution methods in the frequency domain [17] allowing for an in-depth characterization of such system's nonlinear response [18, 19, 20].

However, due to specific theoretical or modeling challenges, such degree of maturity has not yet been reached for all nonlinear interfaces. In particular, the blade-tip/casing contact interface is characterized by very high relative speeds between the impacting components, the high flexibility of blades and the critical need to accurately model the contact interface in an area where nominal clearances are extremely small [21]. The numerical severity of unilateral contacts occurring at this interface [22], yielding a highly nonlinear mechanical system, has made it more difficult to use frequency methods [23, 24, 25] and only a handful of numerical investigations attempted to carry out stability analyses for the blade-tip/casing interface [25, 26, 27]. This represents a significant roadblock for designers who are facing blade-tip/casing interactions in potentially any stage of an engine with both radial [11] and axial geometries [28]. This also prevents the development of comprehensive numerical strategies dedicated to the combined analysis of several nonlinear interfaces combined.

To this day, researchers relied mostly on numerical time integration [29] (TI) for the prediction of blade-tip/casing contacts interactions [30, 8]. This choice was motivated by several factors: (1) it was originally assumed that a very accurate contact treatment algorithm was required to obtain physically relevant results [31], and (2) experimental studies highlighted that witnessed interactions are often related to transient or diverging motions. Yet, numerical time integration entails costly numerical simulations in terms of computation times which prevents its use for a qualitative characterization of nonlinear interactions. This has motivated the development of frequency domain methods dedicated to handling blade/casing contact interactions. In a recent article [22], it was shown that a harmonic balance method (HBM)-based approach combined with a specific regularization of the contact law and Lanczos filtering of nonlinear forces was well-suited for the analysis of blade-tip/casing interactions. In particular, Lanczos filtering efficiently mitigates the Gibbs phenomenon thus significantly enhancing the convergence of the iterative solver. In order to demonstrate the potential of this methodology—namely the RL-HBM (Regularized Lanczos HBM)—in an industrial context, it was shown that it yields results in good agreement with TI reference numerical strategies. Most importantly, the RL-HBM allows for an accurate and numerically efficient estimation of a blade's nonlinear resonance.

Yet, the qualitative understanding of a nonlinear mechanical system's dynamics calls for an accurate assessment of the local stability of the computed solutions. While there exists several numerical methods to achieve this [32, 33], their applicability and their efficiency significantly depends on the type of nonlinearity the system is subjected to [34]. For phenomenological mechanical systems featuring smooth nonlinearities (and, oftentimes, high structural damping values), there have been many numerical developments providing insight on the system's response and stability boundaries in the parameter space [35, 19, 27, 36, 20]. In the case of unilateral contact constraints on industrial

models with low structural damping however, specific challenges arise that have not yet been fully addressed. Besides of the inherent numerical complexity of stability assessment, contact nonlinearities yield an intricate dynamics with many bifurcation points for which numerical accuracy and robustness of the solver become critical [25, 27, 36].

The present article focuses on the stability analysis of mechanical systems undergoing contact nonlinearities and the influence of Lanczos filtering on stability assessment. The RL-HBM is used to compute the response of several mechanical systems of increasing complexity: from a single-degree of freedom impactor with a fixed and moving obstacle to an industrial compressor blade in contact with its surrounding casing accounting for friction. In the first section of the article, the numerical framework is introduced. The two considered solution paradigms are presented: in the time domain a reference TI methodology is briefly recalled, and key features of the RL-HBM are reminded in the frequency domain. Particular attention is paid to the expression of the Jacobian matrices that are derived analytically to ensure the numerical robustness of the solver and the accuracy of the resulting stability analysis. Then, section 3 provides key points of Floquet theory for the stability assessment of predicted solutions and the two methodologies considered in the article, namely the Newmark $2n$-pass method and Hill's method are introduced and validated on phenomenological models. Finally, in section 4, the stability analyses of periodic solutions computed with the RL-HBM for a single degree of freedom impactor and an industrial blade undergoing contact interactions are carried out, with an emphasis on the influence of Lanczos filtering on the presented results.

2 Numerical Framework

The equation of motion of a n-dof nonlinear mechanical system reads:

$$\mathbf{M}\ddot{\boldsymbol{x}}(t) + \mathbf{C}\dot{\boldsymbol{x}}(t) + \mathbf{K}\boldsymbol{x}(t) + \boldsymbol{f}_{\text{nl}}(\boldsymbol{x}(t), \dot{\boldsymbol{x}}(t), \omega) = \boldsymbol{f}_{\text{ext}}(t, \omega) \tag{1}$$

where $\mathbf{M}$, $\mathbf{C}$, $\mathbf{K}$ are the mass, damping and stiffness matrices, $\boldsymbol{x}$ is the displacement vector, $\boldsymbol{f}_{\text{nl}}$ is the nonlinear forces vector and $\boldsymbol{f}_{\text{ext}}$ corresponds to the periodic excitation forces of angular frequency ω. The dot notation refers to derivatives with respect to time t. All the developments presented hereafter may easily be extended to the case where $\boldsymbol{f}_{\text{nl}}$ also depends on $\ddot{\boldsymbol{x}}$ [26].

In order to solve Eq. (1) in the context of blade-tip casing interactions, two solution paradigms may be considered: time and frequency domain. In this paper, only key equations of TI, used for validation purposes only, are recalled for the sake of completeness.

2.1 Time domain

The employed time integration algorithm [29] combines a central finite difference scheme with a Lagrange multipliers-based contact management. Equation (1) is solved at each time step t_i using a prediction/correction approach. Predicted displacements $\boldsymbol{x}^{\text{p}}$ at time t_{i+1} are:

$$\boldsymbol{x}^{\text{p}}(t_{i+1}) = \left(\frac{\mathbf{M}}{h^2} + \frac{\mathbf{C}}{2h}\right)^{-1} \left[\left(\frac{2\mathbf{M}}{h^2} - \mathbf{K}\right)\boldsymbol{x}(t_i) + \left(\frac{\mathbf{C}}{2h} - \frac{\mathbf{M}}{h^2}\right)\boldsymbol{x}(t_{i-1})\right] \tag{2}$$

where h is the time step. Should contact be detected, a correction is applied in order to satisfy contact constraints:

$$\boldsymbol{x}(t_{i+1}) = \boldsymbol{x}^{\text{p}}(t_{i+1}) + \left(\frac{\mathbf{M}}{h^2} + \frac{\mathbf{D}}{2h}\right)^{-1} \boldsymbol{\lambda} \tag{3}$$

where $\boldsymbol{\lambda}$ are the Lagrange multipliers representing the normal contact forces, computed using the predicted penetration between the blade and the casing.

2.2 Frequency domain

Key equations of the HBM are recalled in A for the sake of completeness. In the remainder of this subsection, only equations specific to the RL-HBM are presented.

2.2.1 Regularization of contact forces

The first step towards the computation of contact forces is the definition of the gap function $\boldsymbol{g}$ as the signed distance between contact nodes and an obstacle:

$$\boldsymbol{g}(t) = \boldsymbol{x}(t) - \boldsymbol{d}(t) \tag{4}$$

where $\boldsymbol{d}(t)$ refers to the time-dependent position of the obstacle. In a HBM framework, contact forces are usually computed by using a penalty method in which the normal component $\boldsymbol{f}_n$ of the nonlinear forces $\boldsymbol{f}_{nl}$ is computed as follows:

$$\boldsymbol{f}_{\mathrm{n}}(t) = \kappa \max\left(\boldsymbol{0}, \boldsymbol{g}(t)\right) \tag{5}$$

where $\kappa \in \mathbb{R}_+$ is the penalty coefficient and the $\max(\cdot,\cdot)$ function provides a pairwise maximum of two vectors. The penalty coefficient should be large enough to prevent significant interpenetrations between the structures. However, it cannot be too high as this would yield an ill-conditioned numerical problem in Eq. (51). Considering a regularization [22] of the activation function $\max\left(\boldsymbol{0}, \boldsymbol{g}(t)\right)$ significantly enhances the robustness of the solver by smoothing contact state transition so that normal components of contact forces may be rewritten as:

$$f_{\mathrm{n},j}(t) = \kappa\frac{g_j(t)}{2} + \sqrt{\left(\kappa\frac{g_j(t)}{2}\right)^2 + \gamma^2} \tag{6}$$

where $\gamma \in \mathbb{R}_+$ acts as a smoothing coefficient, and $f_{\mathrm{n},j}$ and g_j respectively refer to the coordinates of vectors $\boldsymbol{f}_{\mathrm{n}}$ and $\boldsymbol{g}$ relatively to the j-th contact node. One may note that Eqs. (5) and (6) are fully equivalent when $\gamma = 0$. For turbomachinery applications, contact forces are usually expressed in a cylindrical coordinate system (r, θ, z) in which the normal contact forces are associated with the radial direction. Radial components are given by the regularized penalty law (6):

$$f_{3j-2,i} = \kappa\frac{g_{j,i}}{2} + \sqrt{\left(\kappa\frac{g_{j,i}}{2}\right)^2 + \gamma^2} \quad \text{for } j \in [\![1..n_{\mathrm{b}}]\!],\ i \in [\![0..N-1]\!] \tag{7}$$

where n_{b} is the considered number of boundary nodes and N is the number of nondimensional time samples, so that $\tau = \omega t$ or, in a discretized form, $\tau_i = 2\pi\frac{i}{N}$ for $i \in [\![0..N-1]\!]$, used to evaluate contact forces within the Alternating Frequency/Time (AFT) scheme in the time domain, recalled in A. Therefore, taking dry friction into account through the Coulomb law implies the existence of a component of the contact force in the plane orthogonal to the radial direction, distributed between the tangential direction:

$$f_{3j-1,i} = \mu\frac{\dot{x}_{3j-1,i} + r_j\omega}{\sqrt{\left(\dot{x}_{3j-1,i} + r_j\omega\right)^2 + \dot{x}_{3j,i}^2}} f_{3j-2,i} = \mu_{3j-1,i} f_{3j-2,i} \quad \text{for } j \in [\![1..n_{\mathrm{b}}]\!],\ i \in [\![0..N-1]\!] \tag{8}$$

and the axial one:

$$f_{3j,i} = \mu\frac{\dot{x}_{3j,i}}{\sqrt{\left(\dot{x}_{3j-1,i} + r_j\omega\right)^2 + \dot{x}_{3j,i}^2}} f_{3j-2,i} = \mu_{3j,i} f_{3j-2,i} \quad \text{for } j \in [\![1..n_{\mathrm{b}}]\!],\ i \in [\![0..N-1]\!] \tag{9}$$

where μ is the friction coefficient such as $\sqrt{\mu_{3j-1,i}^2 + \mu_{3j,i}^2} = \mu$, and where $\dot{x}_{3j-1,i}$, $\dot{x}_{3j,i}$ and r_j are respectively the tangential velocity, the axial velocity and the radial position of the j-th boundary node. Sliding conditions are assumed at all time due to the very high relative speed between the blade-tip and the casing.

2.2.2 Computation of the Jacobian matrices

The analytical expressions of contact forces allow to evaluate the partial derivatives relative to each contact node of the system in order to construct the time-domain Jacobian matrices extended over one period of motion diagonally

$\partial \hat{\boldsymbol{f}}_{\mathrm{nl}}/\partial \boldsymbol{x}$ and $\partial \hat{\boldsymbol{f}}_{\mathrm{nl}}/\partial \dot{\boldsymbol{x}}$ by blocks. The j-th block, of dimension $(3N \times 3N)$, of the Jacobian of the nonlinear forces with respect to the displacements of the j-th the boundary node has the following structure:

$$\frac{\partial \hat{\boldsymbol{f}}_j}{\partial \boldsymbol{x}_j} = \begin{bmatrix} \mathrm{diag}\left(\dfrac{\partial \boldsymbol{f}_{3j-2}}{\partial \boldsymbol{x}_{3j-2}}\right) & \mathrm{diag}\left(\dfrac{\partial \boldsymbol{f}_{3j-2}}{\partial \boldsymbol{x}_{3j-1}}\right) & \mathrm{diag}\left(\dfrac{\partial \boldsymbol{f}_{3j-2}}{\partial \boldsymbol{x}_{3j}}\right) \\ \mathrm{diag}\left(\dfrac{\partial \boldsymbol{f}_{3j-1}}{\partial \boldsymbol{x}_{3j-2}}\right) & \mathrm{diag}\left(\dfrac{\partial \boldsymbol{f}_{3j-1}}{\partial \boldsymbol{x}_{3j-1}}\right) & \mathrm{diag}\left(\dfrac{\partial \boldsymbol{f}_{3j-1}}{\partial \boldsymbol{x}_{3j}}\right) \\ \mathrm{diag}\left(\dfrac{\partial \boldsymbol{f}_{3j}}{\partial \boldsymbol{x}_{3j-2}}\right) & \mathrm{diag}\left(\dfrac{\partial \boldsymbol{f}_{3j}}{\partial \boldsymbol{x}_{3j-1}}\right) & \mathrm{diag}\left(\dfrac{\partial \boldsymbol{f}_{3j}}{\partial \boldsymbol{x}_{3j}}\right) \end{bmatrix} = \begin{bmatrix} \mathrm{diag}\left(\dfrac{\partial \boldsymbol{f}_{3j-2}}{\partial \boldsymbol{x}_{3j-2}}\right) & \boldsymbol{0}_N & \boldsymbol{0}_N \\ \mathrm{diag}\left(\dfrac{\partial \boldsymbol{f}_{3j-1}}{\partial \boldsymbol{x}_{3j-2}}\right) & \boldsymbol{0}_N & \boldsymbol{0}_N \\ \mathrm{diag}\left(\dfrac{\partial \boldsymbol{f}_{3j}}{\partial \boldsymbol{x}_{3j-2}}\right) & \boldsymbol{0}_N & \boldsymbol{0}_N \end{bmatrix} \tag{10}$$

where $\boldsymbol{0}_N$ is the null matrix of size N, and where the nonzero terms associated with the gradients of the nonlinear forces with respect to the radial displacement are defined as:

$$\left.\frac{\partial f_{3j-2}}{\partial x_{3j-2}}\right|_{\tau_i} = \frac{\kappa}{2} + \frac{\kappa^2 g_{j,i}}{2\sqrt{\kappa^2 g_{j,i}^2 + 4\gamma^2}} \tag{11}$$

$$\left.\frac{\partial f_{3j-1}}{\partial x_{3j-2}}\right|_{\tau_i} = \mu_{3j-1,i} \left.\frac{\partial f_{3j-2}}{\partial x_{3j-2}}\right|_{\tau_i} \tag{12}$$

$$\left.\frac{\partial f_{3j}}{\partial x_{3j-2}}\right|_{\tau_i} = \mu_{3j,i} \left.\frac{\partial f_{3j-2}}{\partial x_{3j-2}}\right|_{\tau_i} \tag{13}$$

Similarly, for the Jacobian of the nonlinear forces with respect to the velocities, the j-th block reads:

$$\frac{\partial \hat{\boldsymbol{f}}_j}{\partial \dot{\boldsymbol{x}}_j} = \begin{bmatrix} \mathrm{diag}\left(\dfrac{\partial \boldsymbol{f}_{3j-2}}{\partial \dot{\boldsymbol{x}}_{3j-2}}\right) & \mathrm{diag}\left(\dfrac{\partial \boldsymbol{f}_{3j-2}}{\partial \dot{\boldsymbol{x}}_{3j-1}}\right) & \mathrm{diag}\left(\dfrac{\partial \boldsymbol{f}_{3j-2}}{\partial \dot{\boldsymbol{x}}_{3j}}\right) \\ \mathrm{diag}\left(\dfrac{\partial \boldsymbol{f}_{3j-1}}{\partial \dot{\boldsymbol{x}}_{3j-2}}\right) & \mathrm{diag}\left(\dfrac{\partial \boldsymbol{f}_{3j-1}}{\partial \dot{\boldsymbol{x}}_{3j-1}}\right) & \mathrm{diag}\left(\dfrac{\partial \boldsymbol{f}_{3j-1}}{\partial \dot{\boldsymbol{x}}_{3j}}\right) \\ \mathrm{diag}\left(\dfrac{\partial \boldsymbol{f}_{3j}}{\partial \dot{\boldsymbol{x}}_{3j-2}}\right) & \mathrm{diag}\left(\dfrac{\partial \boldsymbol{f}_{3j}}{\partial \dot{\boldsymbol{x}}_{3j-1}}\right) & \mathrm{diag}\left(\dfrac{\partial \boldsymbol{f}_{3j}}{\partial \dot{\boldsymbol{x}}_{3j}}\right) \end{bmatrix} = \begin{bmatrix} \boldsymbol{0}_N & \boldsymbol{0}_N & \boldsymbol{0}_N \\ \boldsymbol{0}_N & \mathrm{diag}\left(\dfrac{\partial \boldsymbol{f}_{3j-1}}{\partial \dot{\boldsymbol{x}}_{3j-1}}\right) & \mathrm{diag}\left(\dfrac{\partial \boldsymbol{f}_{3j-1}}{\partial \dot{\boldsymbol{x}}_{3j}}\right) \\ \boldsymbol{0}_N & \mathrm{diag}\left(\dfrac{\partial \boldsymbol{f}_{3j}}{\partial \dot{\boldsymbol{x}}_{3j-1}}\right) & \mathrm{diag}\left(\dfrac{\partial \boldsymbol{f}_{3j}}{\partial \dot{\boldsymbol{x}}_{3j}}\right) \end{bmatrix} \tag{14}$$

with the following gradients of the nonlinear tangential and axial forces with respect to the associated nonzero velocities:

$$\left.\frac{\partial f_{3j-1}}{\partial \dot{x}_{3j-1}}\right|_{\tau_i} = \mu \frac{\dot{x}_{3j,i}^2}{\left(\left(\dot{x}_{3j-1,i} + r_j\omega\right)^2 + \dot{x}_{3j,i}^2\right)^{3/2}} f_{3j-2,i} \tag{15}$$

$$\left.\frac{\partial f_{3j}}{\partial \dot{x}_{3j}}\right|_{\tau_i} = \mu \frac{\left(\dot{x}_{3j-1,i} + r_j\omega\right)^2}{\left(\left(\dot{x}_{3j-1,i} + r_j\omega\right)^2 + \dot{x}_{3j,i}^2\right)^{3/2}} f_{3j-2,i} \tag{16}$$

$$\left.\frac{\partial f_{3j-1}}{\partial \dot{x}_{3j}}\right|_{\tau_i} = \left.\frac{\partial f_{3j}}{\partial \dot{x}_{3j-1}}\right|_{\tau_i} = -\mu \frac{\left(\dot{x}_{3j-1,i} + r_j\omega\right)\dot{x}_{3j-1}}{\left(\left(\dot{x}_{3j-1,i} + r_j\omega\right)^2 + \dot{x}_{3j,i}^2\right)^{3/2}} f_{3j-2,i} \tag{17}$$

This yields the evaluation of seven nonzero partial derivatives of the contact forces, with respect to displacements and velocities, for each nonlinear node. Contrary to the radial forces (Eq. (7)), tangential (Eq. (8)) and axial forces (Eq. (9)) depend on the angular velocity ω. For that reason the computation of the associated gradients when considering a non-natural continuation parameterization is required (*e.g.* arc-length parameterization):

$$\left.\frac{\partial f_{3j-1}}{\partial \omega}\right|_{\tau_i} = \mu \frac{r_j \dot{x}_{3j,i}^2}{\left(\left(\dot{x}_{3j-1,i} + r_j\omega\right)^2 + \dot{x}_{3j,i}^2\right)^{3/2}} f_{3j-2,i} \tag{18}$$

$$\left.\frac{\partial f_{3j}}{\partial \omega}\right|_{\tau_i} = -\mu \frac{r_j \dot{x}_{3j-1}\left(\dot{x}_{3j-1,i} + r_j\omega\right)}{\left(\left(\dot{x}_{3j-1,i} + r_j\omega\right)^2 + \dot{x}_{3j,i}^2\right)^{3/2}} f_{3j-2,i} \tag{19}$$

Finally, the frequency-domain nonlinear forces Jacobian matrix $\partial \tilde{\boldsymbol{f}}_{\mathrm{nl}}(\tilde{\boldsymbol{x}})/\partial \tilde{\boldsymbol{x}}$ of Eq. (56) may be expressed semi-analytically using the chain rule and linearity property of the DFT operators (forward $\boldsymbol{\Gamma}^{-1}$ and inverse $\boldsymbol{\Gamma}$), see [22, 1], as:

$$\frac{\partial \tilde{\boldsymbol{f}}_{\mathrm{nl}}(\tilde{\boldsymbol{x}},\omega)}{\partial \tilde{\boldsymbol{x}}} = \frac{\partial \tilde{\boldsymbol{f}}_{\mathrm{nl}}}{\partial \boldsymbol{f}_{\mathrm{nl}}}\frac{\partial \boldsymbol{f}_{\mathrm{nl}}}{\partial \boldsymbol{x}}\frac{\partial \boldsymbol{x}}{\partial \tilde{\boldsymbol{x}}} + \frac{\partial \tilde{\boldsymbol{f}}_{\mathrm{nl}}}{\partial \boldsymbol{f}_{\mathrm{nl}}}\frac{\partial \boldsymbol{f}_{\mathrm{nl}}}{\partial \dot{\boldsymbol{x}}}\frac{\partial \dot{\boldsymbol{x}}}{\partial \tilde{\boldsymbol{x}}} = \boldsymbol{\Gamma}^{-1}\frac{\partial \hat{\boldsymbol{f}}_{\mathrm{nl}}}{\partial \boldsymbol{x}}\boldsymbol{\Gamma} + \boldsymbol{\Gamma}^{-1}\frac{\partial \hat{\boldsymbol{f}}_{\mathrm{nl}}}{\partial \dot{\boldsymbol{x}}}\boldsymbol{\Gamma}(\omega\boldsymbol{\nabla}\otimes\mathbf{I}_n) \tag{20}$$

where $\partial \hat{\boldsymbol{f}}_{\mathrm{nl}}/\partial \boldsymbol{x}$ and $\partial \hat{\boldsymbol{f}}_{\mathrm{nl}}/\partial \dot{\boldsymbol{x}}$ are the sought diagonally extended Jacobian matrices of dimension $(3n_{\mathrm{b}}N \times 3n_{\mathrm{b}}N)$ constructed from every boundary node block matrices of Eqs. (10) and (14) such as:

$$\frac{\partial \hat{\boldsymbol{f}}_{\mathrm{nl}}}{\partial \boldsymbol{x}} = \mathrm{diagblock}\left(\frac{\partial \hat{\boldsymbol{f}}_1}{\partial \boldsymbol{x}_1}, \ldots, \frac{\partial \hat{\boldsymbol{f}}_{n_{\mathrm{b}}}}{\partial \boldsymbol{x}_{n_{\mathrm{b}}}}\right) \quad \text{and} \quad \frac{\partial \hat{\boldsymbol{f}}_{\mathrm{nl}}}{\partial \dot{\boldsymbol{x}}} = \mathrm{diagblock}\left(\frac{\partial \hat{\boldsymbol{f}}_1}{\partial \dot{\boldsymbol{x}}_1}, \ldots, \frac{\partial \hat{\boldsymbol{f}}_{n_{\mathrm{b}}}}{\partial \dot{\boldsymbol{x}}_{n_{\mathrm{b}}}}\right) \tag{21}$$

When compared to finite difference approximations, the computation of analytical derivatives not only yields a substantial speedup in gradient-based numerical root-finding algorithms but also increases the accuracy of the resulting frequency domain Jacobian matrix $\mathbf{R}_{,\tilde{\boldsymbol{x}}}$ defined in Eq. (56), thus enhancing the convergence of the solver [37]. Moreover, the accuracy of these derivatives is of the utmost importance when a local stability analysis is carried out upon the converged solutions, see section 3.

2.2.3 Lanczos filtering

Although the regularization of the contact law improves the numerical robustness of the solver, it is found to have negligible impact on the Gibbs phenomenon when considering $\gamma \ll \kappa$. The RL-HBM relies on a second order Lanczos filter (also known as σ-approximation or Lanczos σ-averaging) [38]. Filtering can be shown as equivalent to introducing a decaying multiplicative factor to nonlinear forces $\boldsymbol{f}_{\mathrm{nl}}$ in Fourier space, so that:

$$\boldsymbol{f}_{\mathrm{nl}}(\boldsymbol{x},\dot{\boldsymbol{x}},\omega) \simeq \frac{1}{2}\boldsymbol{a}_0^{\mathrm{nl}} + \sum_{j=1}^{H} \sigma_j \left[\boldsymbol{a}_j^{\mathrm{nl}}\cos(j\omega t) + \boldsymbol{b}_j^{\mathrm{nl}}\sin(j\omega t)\right] \tag{22}$$

where:

$$\sigma_j = \mathrm{sinc}(\mathcal{X}_j)^m \quad \text{with} \quad \mathcal{X}_j = \begin{cases} 0 & \text{for } j < C_H \\ \frac{j}{H+1} & \text{for } C_H \leq j \leq H \end{cases} \tag{23}$$

Coefficients σ_j are the Lanczos factors given that $\mathrm{sinc}(\cdot)$ is the normalized cardinal sine function and $m \in \mathbb{R}_+$ is a smoothing exponent that controls the intensity of the filter by allowing to perform m-repeated Lanczos averagings [38, 39]. Parameter $\mathcal{X}_j$ controls the intensity of filtering for each harmonic of the truncated Fourier series based on the cut-off harmonic C_H that allows to control the onset of the filtering window. The effect of a unitary ($m = C_H = 1$) Lanczos filter (——) is illustrated in Fig. 1 for an impact-like truncated sine function defined as $\boldsymbol{f}_{\mathrm{nl}}(x(t)) = 10^3 \max(0, \cos(\omega t + \pi) - 0.8)$. One may see that spurious oscillations are considerably attenuated, and even more for its first-order derivative with respect to the displacements, but rising time near the discontinuities is increased when compared to the unfiltered case (——).

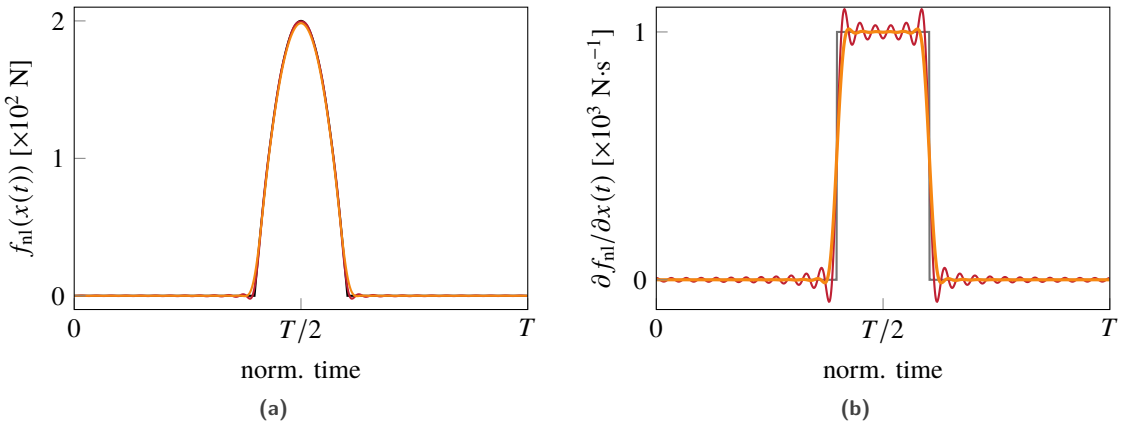

Figure 1 – Impact-like function (——) and its first-order derivative with respect to the displacement (——). Fourier approximation ($H = 30$) (——) and Fourier approximation with Lanczos filtering (——) are superimposed.

3 Stability analysis of periodic solutions

When coupled with a continuation procedure, the RL-HBM yields indistinctly both stable and unstable solutions, it is thus required to assess their stability *a posteriori*. In this section, different strategies to assess the local stability of periodic solutions are recalled. These methods consist in assessing the influence of a small perturbation to a periodic solution of the equation of motion over time.

3.1 Academic impactor

For validation purposes, a single dof oscillator subjected to unilateral contact constraints, illustrated in Fig. 2, is considered throughout this section. This type of impactor [40, 41] is rarely considered in the literature within a frequency-domain framework as contact nonlinearities are numerically more challenging [42, 34] when compared to smooth nonlinearities which are often favored to demonstrate stability analyses [19, 43, 44]. To the best of the authors' knowledge, it is the first time that stability of the solutions of such an impactor is assessed using both time and frequency-domain algorithms.

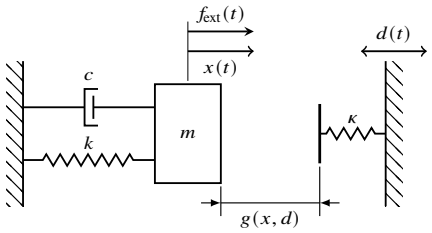

Figure 2 – Schematic representation of the considered impactor.

The impactor is characterized by its mass $m = 1$ kg, stiffness $k = 1$ N·m^{-1}, and modal damping coefficient $\xi = c/2\sqrt{km} = 5 \cdot 10^{-2}$. The dynamic response of the impactor is studied in the vicinity of its natural resonance frequency ω_0. In sections 2 and 3, all presented results are obtained with $H = 30$ and $N = 1024$. These values were selected following a careful convergence analysis, not detailed here for the sake of brevity.

3.2 Floquet Theory

3.2.1 Principle

Key equations related to Floquet Theory [45] are recalled for the sake of completeness. Given the general equation of a continuous-time dynamical system in the state space:

$$\dot{\boldsymbol{z}} = \boldsymbol{G}(\boldsymbol{z}, t, \lambda),\ \boldsymbol{G} : \mathbb{R}^{2n} \times \mathbb{R} \times \mathbb{R} \to \mathbb{R}^{2n} \quad \text{with} \quad \boldsymbol{z}(t) = \begin{bmatrix} \boldsymbol{x}(t) \\ \dot{\boldsymbol{x}}(t) \end{bmatrix} \tag{24}$$

Assuming $\boldsymbol{z}^\star(t)$ is a T-periodic solution of Eq. (24) related to a fixed control parameter $\lambda = \lambda^\star$, the assessment of its stability relies on its summation with a small perturbation $\boldsymbol{y}(t)$:

$$\boldsymbol{z}(t) = \boldsymbol{z}^\star(t) + \boldsymbol{y}(t) \tag{25}$$

The combination of Eq. (25) and Eq. (24), along with the expansion of the resulting equation into a Taylor series in $\boldsymbol{z}^\star$, yields the following linear ordinary differential equation system with periodically time-varying coefficients:

$$\dot{\boldsymbol{y}}(t) = \mathbf{J}(\boldsymbol{z}^\star, t)\boldsymbol{y}(t) \tag{26}$$

where $\mathbf{J}$ is the state space Jacobian matrix of $\boldsymbol{G}$ evaluated at $\boldsymbol{z}^\star$. The Floquet theory then shows that for any $m \in [\![1..2n]\!]$, the solution of Eq. (26), namely $\boldsymbol{y}(t)$, is the sum of $2n$ linearly independent fundamental solutions $\boldsymbol{y}_m(t)$:

$$\boldsymbol{y}(t) = \sum_{m=1}^{2n} \boldsymbol{y}_m(t) \quad \text{with :} \quad \boldsymbol{y}_m(t) = \boldsymbol{p}_m(t)\, \mathrm{e}^{\alpha_m t},\ \boldsymbol{p}_m\ T\text{-periodic},\ \alpha_m \in \mathbb{C} \tag{27}$$

where α_m are the Floquet exponents defined uniquely modulo $2\mathrm{i}\pi/T$ and $\boldsymbol{p}_m$ are complex vectors. Rewriting Eq. (27) in matricial form considering $\boldsymbol{Y}(t) = [\boldsymbol{y}_1(t),\ \ldots,\ \boldsymbol{y}_{2n}(t)]$, it now reads:

$$\dot{\boldsymbol{Y}}(t) = \mathbf{J}(\boldsymbol{z}^\star, t)\boldsymbol{Y}(t) \tag{28}$$

With the change of variable $\bar{t} = t + T$, this equation becomes:

$$\frac{d\boldsymbol{Y}}{d\bar{t}} = \mathbf{J}(\boldsymbol{z}^\star, \bar{t} - T)\boldsymbol{Y}(\bar{t} - T) = \mathbf{J}(\boldsymbol{z}^\star, \bar{t})\boldsymbol{Y}(\bar{t}) \tag{29}$$

Therefore, if $\boldsymbol{Y}(t)$ is a fundamental matrix of solutions, then so is $\boldsymbol{Y}(t+T)$. However, because Eq. (26) admits at most only $2n$ linearly independent solutions, the solutions $\boldsymbol{y}_m(t+T)$ are necessarily linear combinations of $\boldsymbol{y}_m(t)$, hence:

$$\forall t\ :\ \boldsymbol{Y}(t+T) = \mathcal{M}\boldsymbol{Y}(t) \tag{30}$$

where $\mathcal{M}$ is the so-called monodromy matrix, or Floquet transition matrix [45, 32]. The monodromy matrix allows to assess the local stability of the periodic solution $\boldsymbol{z}^\star$ as it maps a particular set of fundamental solutions $\boldsymbol{Y}(t)$ to their values at $t+T$. One may note that $\mathcal{M}$ depends on the choice of the fundamental matrix $\boldsymbol{Y}(t)$ and is therefore not unique. Nevertheless, one can choose to impose as initial conditions:

$$\boldsymbol{Y}(0) = \frac{\partial \boldsymbol{G}(\boldsymbol{z}^\star, 0, \lambda^\star)}{\partial \boldsymbol{z}^\star} = \frac{\partial \boldsymbol{z}^\star}{\partial \boldsymbol{z}^\star} = \mathbf{I}_{2n} \tag{31}$$

which simplifies Eq. (30), and yields:

$$\mathcal{M} = \boldsymbol{Y}(T) \tag{32}$$

The eigenvalues ρ_m of $\mathcal{M}$, called the Floquet multipliers, are unique, and linked to the exponents α_m by the following relations:

$$\rho_m = \mathrm{e}^{\alpha_m T} \Leftrightarrow \alpha_m = \frac{1}{T}\ln(|\rho_m|) + \mathrm{i}\frac{\arg(\rho_m) + 2k\pi}{T},\ k \in \mathbb{Z} \tag{33}$$

It is then possible to define the stability of a periodic solution $\boldsymbol{z}^\star$ with respect to the Floquet exponents and multipliers so that if at least one of the Floquet exponents has a positive real part, the solution is unstable, otherwise it is asymptotically stable. Similarly, should the modulus of one of the Floquet multipliers be greater than one, the solution would be unstable, but stable if not. In a nutshell, a solution is stable if it survives small perturbations. In reality, small perturbations may relate, for instance, to an imperfect excitation. From a numerical standpoint, these perturbations may be related to finite numerical precision errors. As a result, if a predicted solution is unstable, it should rather be seen as a mathematical equilibrium than a solution that can be physically encountered in reality.

3.2.2 Bifurcations of codimension-1

The mechanisms for the change of local stability of a periodic solution with respect to the variation of only one control parameter λ are here presented. Critical points where these changes occur, called bifurcations of codimension-1, can be classified into two main categories [46] with four distinct scenarios.

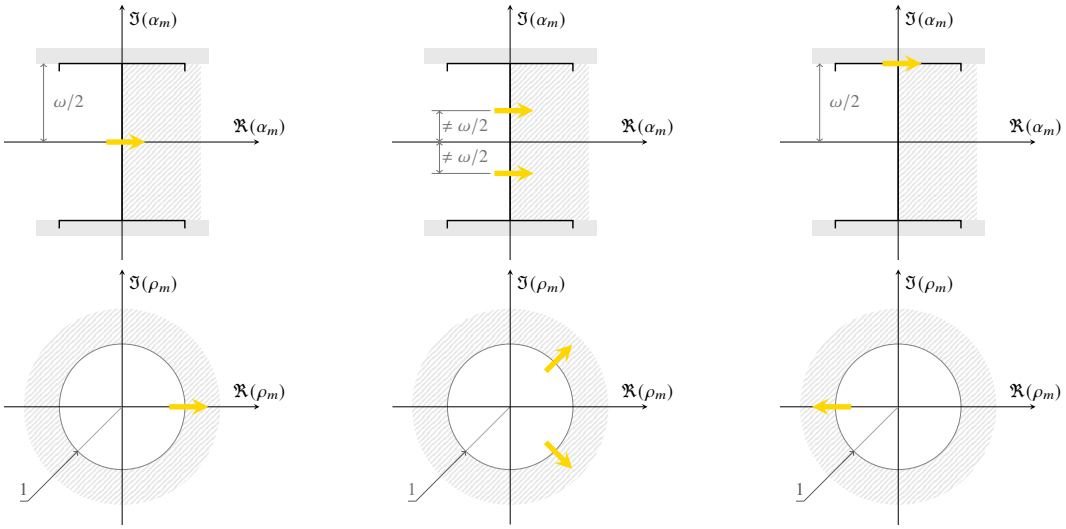

Figure 3 – Bifurcation scenarios for the Floquet exponents (top row, crossing of the imaginary axis) and for the Floquet multipliers (bottom row, path taken when crossing the unit circle): (a) limit point, (b) Neimark-Sacker bifurcation, (c) period doubling bifurcation.

Static bifurcations (SB) occur when a Floquet multiplier is outside the unit circle of the complex plane along the real axis through $+1$ or, analogously, when a Floquet exponent crosses the imaginary axis at 0, see Fig. 3a. In the HBM framework, these bifurcations correspond to a singularity of the Jacobian matrix $\mathbf{R}_{,\tilde{\boldsymbol{x}}}$. Generally, these bifurcations are limit points which are characterized by the presence of a vertical tangent on the NFRC. In the degenerate case (indicating the non-uniqueness of this tangent), these bifurcations correspond to a branch point, where two branches of solutions intersect with apparition of a symmetry-breaking phenomenon. At a branch point, one may solve the well-known algebraic branching equation [47, 48, 36] to compute the two distinct tangents associated with the current branch and the intersecting one.
Dynamic bifurcations includes Neimark-Sacker (NS) (also called secondary Hopf) and period doubling (PD) bifurcations. Neimark-Sacker bifurcations arise when a pair of Floquet multipliers leaves the unit circle as complex

conjugates or, alternatively, when a pair of Floquet exponents crosses the imaginary axis by any value $|\beta| \in]0, \omega/2[$, see Fig. 3b. If $\omega/\beta \notin \mathbb{Q}$, the new branch of solutions is quasi-periodic, alternately, if $\omega/\beta \in \mathbb{Q}$, then the branching solutions is βT-periodic. A period doubling bifurcation is evidenced when a single Floquet multiplier leaves the unit circle along the real axis by -1 or, similarly, when a Floquet exponent crosses the imaginary axis in $\omega/2$, see Fig. 3c. When performing numerical continuation, bifurcations may be detected with scalar test functions [49, 19, 36], bordering techniques [50, 33], or by directly monitoring the Floquet related quantities [47]. In either case, a bifurcation is detected if a sign change occurs for an indicator between two consecutive solutions. Once detected, the location of a bifurcation may be more accurately predicted by solving the residual equilibrium (51) with additional constraint equations [50]. In the remainder, quantities relating to a converged solution are highlighted by $(\star)$.

3.3 Computation of the Floquet exponents in the time domain

There exists several different time-domain algorithms to compute the monodromy matrix [37, 32]. The main numerical challenge relates to finding the best compromise between computational cost and accuracy of the matrix coefficients. Once the monodromy matrix has been computed, its eigendecomposition is not computationally challenging as it only scales with the number of dof n.

3.3.1 Newmark $2n$-pass method

In the Newmark $2n$-pass method, the coefficients of the monodromy matrix $\mathcal{M}$ associated with any system (24) are obtained by integrating $2n$ times the associated linear time-periodic system governing the dynamical perturbation around a periodic stationary state. For Eq. (1), it may be shown [32, 26] that it is equivalent to integrate over one period of motion T the equation:

$$\mathbf{M}\ddot{\boldsymbol{x}}(t) + \left[\mathbf{C} + \left.\frac{\partial \boldsymbol{f}_{\text{nl}}^{\star}}{\partial \dot{\boldsymbol{x}}}\right|_{t=\tau_i}\right]\dot{\boldsymbol{x}}(t) + \left[\mathbf{K} + \left.\frac{\partial \boldsymbol{f}_{\text{nl}}^{\star}}{\partial \boldsymbol{x}}\right|_{t=\tau_i}\right]\boldsymbol{x}(t) = \mathbf{0} \tag{34}$$

Initial conditions to be used are the $2n$ linearly independent initial conditions contained in the state vectors $\boldsymbol{z}_0^{(k)} = [\boldsymbol{x}(t_0),\, \dot{\boldsymbol{x}}(t_0)]^{\top}$ corresponding to the columns of the identity matrix $\mathbf{I}_{2n}$, with $k \in [\![1..2n]\!]$, and where the state space Jacobian matrices of the nonlinear forces at each instant are obtained as a by-product of the AFT cycle associated to the converged solution. The monodromy matrix is thus obtained one column at a time:

$$\mathcal{M} = \left[\ \boldsymbol{z}^{(1)}(T),\ \ldots,\ \boldsymbol{z}^{(k)}(T),\ \ldots,\ \boldsymbol{z}^{(2n)}(T)\ \right] \tag{35}$$

In this work, the implicit Newmark scheme of average acceleration is used to integrate Eq. (34) as it is unconditionally stable for linear systems. In the following, this method is referred to as Newmark $2n$-pass.

3.3.2 Application

A fixed gap ($d(t) = d = 0.8$ m) contact configuration is first considered for the impactor. In this configuration, an external forcing is required to initiate contact. To this end, a monoharmonic external forcing $f_{\text{ext}}(t) = \bar{p}\cos(\omega t)$ is applied by considering a forcing amplitude $\bar{p} = 0.3$ N. The considered contact law parameters of Eq. (6) are $\kappa = 10$ N·m^{-1} and $\gamma = 6 \cdot 10^{-3}$ N. For this application, there is no Lanczos filtering of the nonlinear contact forces.

The Nonlinear Frequency Response Curve (NFRC) obtained with the HBM approach and a stability analysis performed using the Newmark $2n$-pass algorithm is depicted in Fig. 4a. The solid lines (——) represent the stable periodic solutions, while the dashed lines (- - -) indicate the unstable ones. In addition, simulations are also carried out using a TI strategy (○) in order to better emphasize the accuracy of the solutions obtained from the frequency-domain methodology. Starting from null initial conditions along the same frequency range and considering the same regularized penalty law, once a steady state has been reached, the maximum amplitude of vibration is evaluated over the last computed period of motion with respect to the excitation. The linear frequency response function (——) is also shown in order to underline the extent of the contact stiffening phenomenon. Floquet multipliers associated to the nonlinear response are represented in the complex plane in Fig. 4b. Unstable solutions correspond to the multipliers located outside of the unit circle (▨).

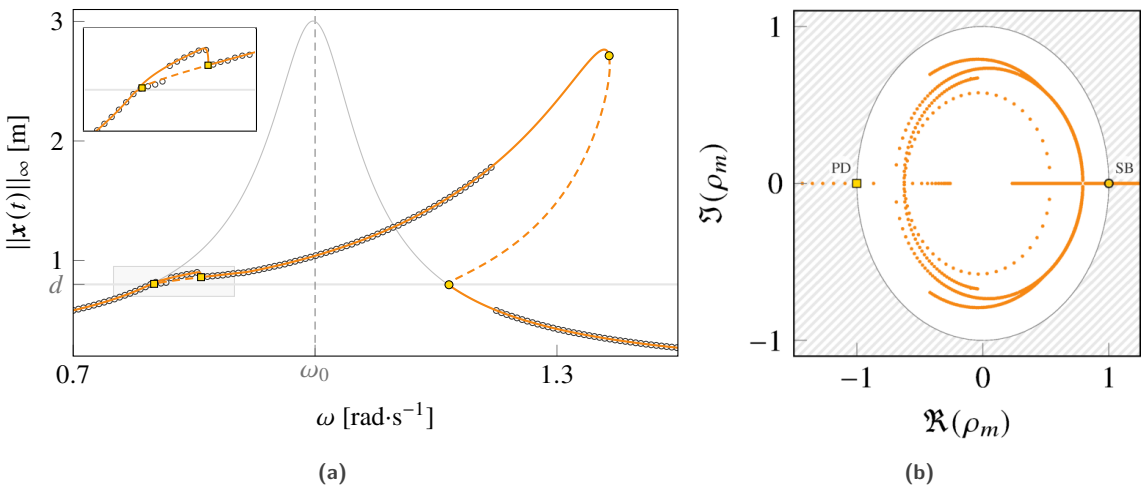

Figure 4 – (a) Nonlinear frequency response curve of the fixed gap single-dof impactor featuring TI results (○), and corresponding (b) Floquet multipliers in the complex plane. Limit points (●) and period doubling bifurcations (■) .

Limit points (●) , evidenced by an exit path of the unit circle in $+1$, and period doubling (■) bifurcations, evidenced by an exit path of the unit circle in -1, are both predicted. Period doubling bifurcations occurring for frequencies lower than the linear resonance, in the area where vibration amplitudes become large enough to initiate contact, are often expected for such fixed gap impactor configuration. They are usually referred to in the literature as grazing-induced bifurcations [41].

The branch of solutions emanating from the period doubling bifurcation (see the zoom in Fig. 4a) can be captured by adding subharmonic functions to the initial Fourier basis. Indeed, subharmonic vibrations may be accounted for with fractional harmonic numbers, such as Eq. (48) now reads:

$$\boldsymbol{x}(t) \simeq \frac{1}{2}\boldsymbol{a}_0 + \sum_{j=1}^{\nu H}\left[\boldsymbol{a}_{j/\nu}\cos\left(\frac{j\omega t}{\nu}\right) + \boldsymbol{b}_{j/\nu}\sin\left(\frac{j\omega t}{\nu}\right)\right] \tag{36}$$

considering a subharmonic ratio $\nu = 2$. In this enriched basis, a period doubling bifurcation now relates to a degenerate static bifurcation: a branch point [47, 36]. Overall, there is an excellent agreement between the $1T$ and $2T$-periodic solutions predicted by HBM and TI.

Real and imaginary parts of the Floquet exponents (●) are pictured in Fig. 5. Floquet exponents with a positive real parts (▨) correspond to unstable solutions, see Fig. 5a. Frequency lock of the imaginary part at $\omega/2$ of one of the Floquet exponents may be seen on the unstable branch between the two period doublings, see Fig. 5b.

3.4 Computation of the Floquet exponents in the frequency domain: Hill's method

3.4.1 Principle

Hill's method is a frequency-domain variant of Floquet theory. In order to assess the stability of a periodic solution, the same procedure as the one described in [17, 33] is applied to the equation of motion which yields the following quadratic eigenvalue problem:

$$(\mathbf{R}^{\star}_{,\tilde{\boldsymbol{x}}} + \boldsymbol{\Delta}_1 s + \boldsymbol{\Delta}_2 s^2)\mathbf{q} = \mathbf{0} \tag{37}$$

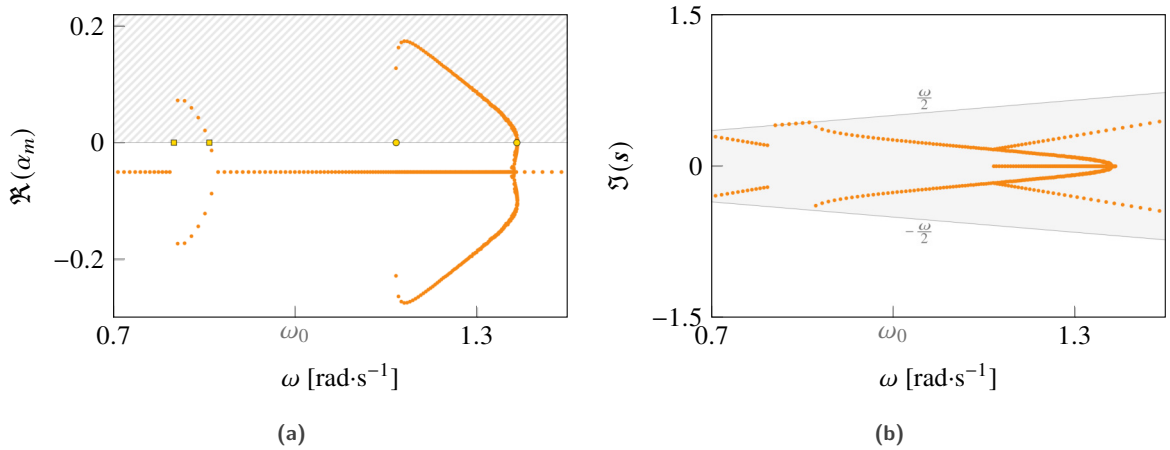

Figure 5 – (a) Real and (b) imaginary parts of Floquet exponents. Limit points (●) and period doubling bifurcations (■) .

where $(s, \mathbf{q})$ are the complex eigensolutions, $\mathbf{R}^{\star}_{,\tilde{\boldsymbol{x}}}$ is the frequency-domain Jacobian matrix defined by Eq. (56) and where the terms $\boldsymbol{\Delta}_1$ and $\boldsymbol{\Delta}_2$ are given by:

$$\begin{aligned} \boldsymbol{\Delta}_1 &= 2\omega^{\star}\boldsymbol{\nabla} \otimes \mathbf{M} + \mathbf{I}_{2H+1} \otimes \mathbf{C} + \boldsymbol{\Gamma}^{-1}\frac{\partial \hat{\boldsymbol{f}}^{\star}_{\mathrm{nl}}}{\partial \dot{\boldsymbol{x}}}\boldsymbol{\Gamma} \\ \boldsymbol{\Delta}_2 &= \mathbf{I}_{2H+1} \otimes \mathbf{M} \end{aligned} \tag{38}$$

where the frequency-domain differentiation operator $\boldsymbol{\nabla}$ is given by Eq. (53). In the particular case where nonlinear forces explicitly depend on the velocities, it should be noted that additional computations are required to obtain the term $\boldsymbol{\Gamma}^{-1}\frac{\partial \hat{\boldsymbol{f}}^{\star}_{\mathrm{nl}}}{\partial \dot{\boldsymbol{x}}}\boldsymbol{\Gamma}$ [26, 27]. From that point, since the Jacobian $\mathbf{R}^{\star}_{,\tilde{\boldsymbol{x}}}$ is already obtained as a by-product of the Newton solver and the terms $\boldsymbol{\Delta}_1$ and $\boldsymbol{\Delta}_2$ are straightforward to evaluate, the main numerical challenge is to solve the quadratic eigenvalue problem (37). To this end, Eq. (37) must be reformulated into an equivalent generalized eigenvalue problem of double size by using a first companion form linearization [51]:

$$\begin{bmatrix} \mathbf{0}_{n_H} & \mathbf{I}_{n_H} \\ -\mathbf{R}^{\star}_{,\tilde{\boldsymbol{x}}} & -\boldsymbol{\Delta}_1 \end{bmatrix} \bar{\mathbf{q}} = s \begin{bmatrix} \mathbf{I}_{n_H} & \mathbf{0}_{n_H} \\ \mathbf{0}_{n_H} & \boldsymbol{\Delta}_2 \end{bmatrix} \bar{\mathbf{q}} \quad \text{with} \quad \bar{\mathbf{q}} = \begin{bmatrix} \mathbf{q} \\ s\mathbf{q} \end{bmatrix} \tag{39}$$

or, equivalently, in a more compact eigendecomposition form:

$$(\mathcal{H} - s\,\mathbf{I}_{2n_H})\,\bar{\mathbf{q}} = \mathbf{0} \quad \text{with} \quad \mathcal{H} = \begin{bmatrix} \mathbf{0}_{n_H} & \mathbf{I}_{n_H} \\ -\boldsymbol{\Delta}_2^{-1}\mathbf{R}^{\star}_{,\tilde{\boldsymbol{x}}} & -\boldsymbol{\Delta}_2^{-1}\boldsymbol{\Delta}_1 \end{bmatrix} \tag{40}$$

Solving Eq. (40) allows to obtain the Hill coefficients $\boldsymbol{s}$ defined as the $L = 2n(2H+1)$ complex eigenvalues of the truncated Hill matrix $\mathcal{H}$ (in its real or trigonometric Fourier representation).

However, there only exists $2n$ eigenvalues among the full set $\boldsymbol{s}$ that approximate the Floquet exponents α_m of the converged solution $\tilde{\boldsymbol{x}}^{\star}$. All the other ones are spurious and are not expected to be of any physical significance. These spurious eigenvalues stem from the truncation of the Fourier series on which the Hill matrix is computed [43]. In addition, no matter the value of the truncation order H is, these spurious eigenvalues will occur so that conducting an analysis over the full raw spectrum of $\mathcal{H}$, *i.e.* considering no sorting, would most often yields an erroneous stability verdict. Moreover, the number of eigenvalues also scales with H. As a result, several sorting algorithms have been proposed in the literature:

Eigenvalue sorting: the $2n$ eigenvalues with smallest imaginary parts in modulus [52, 33] are expected to have a physical meaning and correspond to the Floquet exponents. Its convergence has been rigorously proven as H is increased [53, 54]. Recently, another sorting criterion based on the real part of the eigenvalues has also been proposed [55].
Spectral primitive cell sorting: all Hill eigenvalues located in the spectral primitive cell [43], also referred to as the fundamental strip [53], defined where $-\omega/2 < \Im(s) \leqslant \omega/2$, are assumed to be the Floquet exponents.
Eigenvector sorting: is built upon the analysis of Hill eigenvectors $\mathbf{q}$, and the selection of the ones with the most symmetric spectrum [56, 43, 44], according to the computation of their associated weighted means. The convergence of this sorting algorithm has not yet been mathematically proven. In some cases, it has been shown to be more efficient than the eigenvalues sorting method [43].

In most cases, $2n$ eigenvalues and eigenvectors are to be found in the state space. However, in the presence of period doublings, as an example, for a $2T$-periodic Floquet form, assuming that H provides a sufficiently converged Hill's spectrum, the spectrum of one of the Floquet forms is exactly locked on $\omega/2$. As a consequence, $2n+2$ eigenvalues and eigenvectors meet the eigenvalues and eigenvectors sorting criteria, thus yielding to additional coefficients, hereafter referred to as ambiguous coefficients (●). That is why, for these two criteria, it is also essential to exclude either the lower or upper bound of the primitive cell in order to only retain $2n$ eigenvalues (or eigenvectors) in the case where the imaginary part of one of the complex conjugate spectra lock in $\omega/2 \pm j\omega, j \in [\![0..H]\!]$, see Fig. 3c. In the case of the eigenvectors sorting algorithm, the selected weighted means w_m are the most centered ones satisfying $-1/2 \leq w_m < 1/2$ [43]: the spectral primitive cell criterion is therefore already included. However, this is not the case for the eigenvalues sorting method, it must be emphasized that the $2n$ eigenvalues with smallest imaginary parts in modulus must be *constrained* within $-\omega/2 < \Im(s) \leqslant \omega/2$, or otherwise, this criterion fails in the presence of period doublings [34].

3.4.2 Application

Hill's method is here applied on the fixed gap impactor. Real and imaginary parts of the Hill coefficients (●) as well as the ones of the $2n$ selected Floquet exponents (●) from both eigenvalues and eigenvectors sorting criteria are depicted in Fig. 6.

First, one may see that the Floquet exponents that are returned by the constrained eigenvalues sorting algorithm are a perfect match with the ones obtained with the Newmark $2n$-pass plotted in Fig. 5. If the eigenvalues sorting is not constrained, it is not possible to adequately predict the stability of the solutions of the NFRC between the period doublings. Indeed, Hill coefficients $\boldsymbol{s}$ are not all independent as they verify the relation [44]:

$$s_m^l = \alpha_m + \mathrm{i}l\omega \quad \text{for } l \in [\![-H..H]\!],\ m \in [\![1..2n]\!] \tag{41}$$

A similar property holds for $\mathbf{q}$. Graphically, for a given m, one may see that the $2H+1$ eigenvalues s_m^l associated to α_m appear with the same real part but with and imaginary part shifted $2H+1$ times by an integer multiple of the angular velocity ω. Hence, in the case of period doublings, there is a numerical uncertainty upon the imaginary parts in $\pm\omega/2$ of some of the Hill coefficients.

It has been remarked that selected Hill coefficients based on the spectral primitive cell (□) criterion are equal to those retained by the constrained eigenvalues sorting as long as the Hill's matrix spectrum is sufficiently converged. That is why results associated to this sorting criterion are not presented in the remainder of this section.

With respect to the eigenvectors sorting algorithm, the stability analysis is qualitatively equivalent. Nonetheless, there are some exponents (●) for which $2n+2$ weighted means are found in the primitive cell. In this case, it is therefore not possible to retain only $2n$ exponents in the state space. However, this behaviour is systematically reproduced when encountering period doublings as it will be shown for the next configuration of the impactor in section 4, which makes this sorting robust.

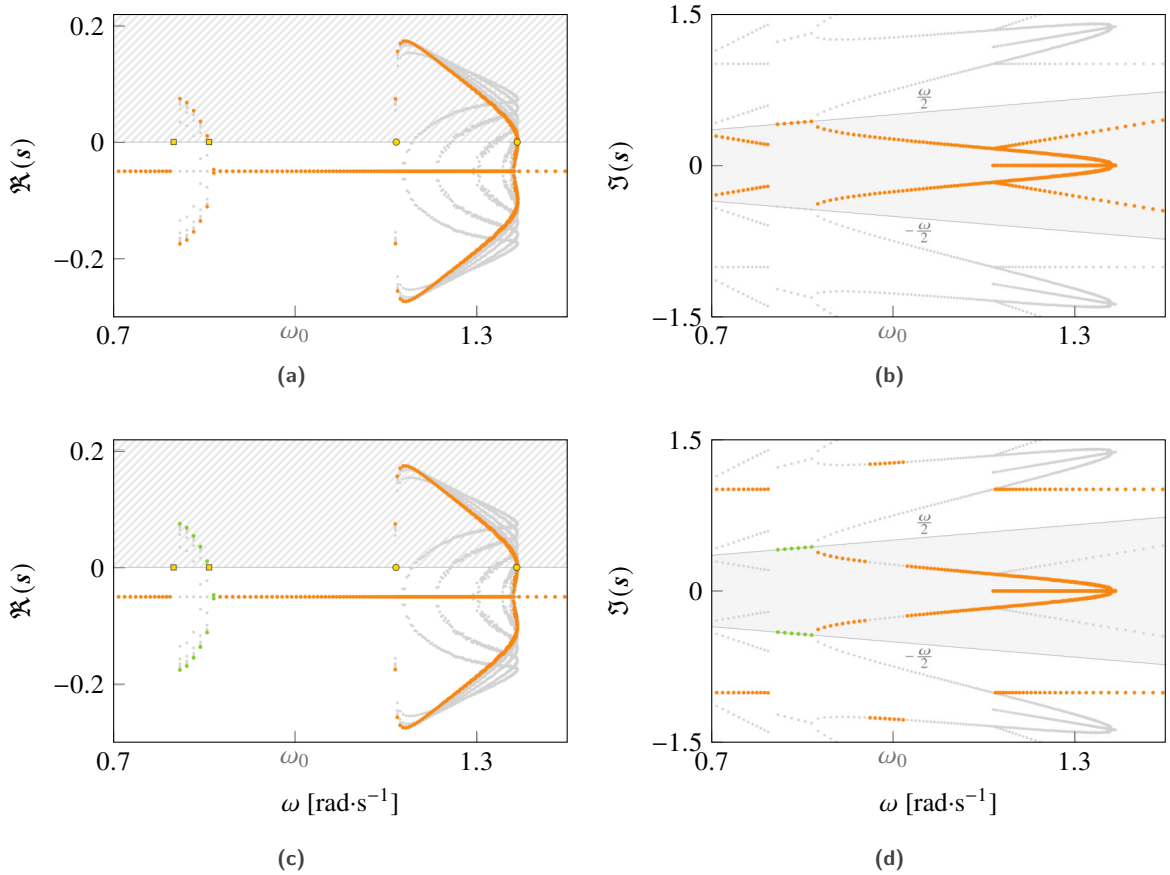

Figure 6 – Real and imaginary parts of Hill coefficients obtained with eigenvalues (a)/(b), and eigenvectors (c)/(d) sorting algorithms. Hill coefficients (●), sorted coefficients (●) and ambiguous coefficients (●). Limit points (●) and period doubling bifurcations (■) .

4 Industrial applications

As mentioned above, the stability analysis of highly nonlinear systems such as those undergoing unilateral contact constraints remains a numerical challenge. From the single-dof impactor considered in the previous section to the industrial case study of interest [22] there are essentially two main differences: the use of a 3D finite element model and the suppression of any linear solution. Putting aside the increased complexity implied by the use of an industrial finite element blade model with a large number of nonlinear dof, the case study of interest [22] features a deformed casing modeled as a time-dependent gap function from a numerical standpoint. The amplitude of the gap function is chosen large enough so that contact will occur for all values of ω. Accordingly, when accounting for a time-dependent gap function, there is no linear solution anymore which yields an increased level of difficulty in terms of numerical solution, specifically to compute the first solution point and initiate the continuation process.

For that reason, the use of a time-dependent gap function, referred to as a moving gap in the remainder, and its consequences in terms the system's dynamics, is first assessed on the single-dof impactor before results are given for the industrial blade.

4.1 Academic impactor with moving gap

The gap function now reads:

$$d_j(\tau_i) = d_{j,i} = a\,(1 + \cos(\tau_i)) - p \tag{42}$$

where a represents the amplitude of the oscillation of the contact threshold, and p is the difference between the position of the mass at rest and the extreme position of the contact threshold. As soon as $p > 0$, structural contacts will occur and there is no linear solution. The considered moving gap features an amplitude of oscillation $a = 10^{-2}$ m and a maximum level of penetration $p = 2 \cdot 10^{-3}$ m. Contact management is performed using Eq. (6) for $\kappa = 100$ N·m^{-1} and $\gamma = 7.5 \cdot 10^{-3}$ N. For this academic impactor, no filtering is employed in the RL-HBM. A careful convergence analysis was conducted: results were found to be converged for $H = 80$ and $N = 2048$. These values are considered throughout this section. In the same way as for the fixed gap contact configuration, TI (○) simulations are also conducted to further validate the RL-HBM and stability results.

4.1.1 Stability analysis

From a numerical standpoint, and in comparison to the stability analysis carried out in the previous section, it is found that the stability analysis is significantly more numerically sensitive with a moving gap. As a matter of fact, the Floquet multiplier which is leaving the unit circle through +1, see Fig. 7b, is associated with two limit points, see Fig. 7a and zoom in Fig. 7c, corresponding to a small superharmonic loop. In the vicinity of this superharmonic resonance, located at $\omega \simeq \omega_0/2$, it is observed that high values of H and N ($H = 80$ and $N = 2048$) are required to precisely compute the nonlinear solutions in order to obtain a perfect agreement between the two stability assessment algorithms. In fact, these results underline that an accurate stability analysis requires significantly higher values of H and N in comparison of those required for an accurate NFRC which is consistent with previous observations in the literature [57]. Floquet exponents obtained using the Newmark $2n$-pass method and Hill's method (real and imaginary parts) are pictured in Fig. 8. For this mechanical system, due to the presence of superharmonic resonances (for $\omega < \omega_0$) and because of the infinitely decaying (yet nonzero) spectrum inherent to contact nonlinearities, sorting algorithms needed in the context of Hill's method are slower to converge. Indeed, secondary resonances require a broader frequency content to be accurately represented. Nonetheless, eigenvalue sorting works flawlessly and is perfectly in line with the results obtained with the Nemark $2n$-pass method, see Figs. 8a and 8c. To the contrary, and similarly to what was observed for the fixed-gap impactor, eigenvector sorting yields ambiguous coefficients (●) located at the lower bound of the frequency range of interest. Though, it should be underlined that this phenomena does not impact the accuracy of the stability assessment.

4.1.2 Precisions on the system's dynamics

The complexity of the nonlinear dynamics induced by the moving gap is now emphasized by narrowing the observations on the period doubling bifurcation located right after the primary nonlinear resonance of the NFRC depicted in Fig. 7a. Successive subharmonic branching, shown in Fig 9, are found. Some selected displacement solutions of T, $2T$, $4T$ and $8T$-periodicity are also depicted in Fig. 9b, see respectively points numbered ① to ④ . This is a clear indication of the presence of a sequence of period doubling bifurcations, one of the routes leading to chaos [58]. This assumption has been verified by using TI (using the same contact law) at $\omega = 2.5$ rad·s^{-1}. The resulting solution is analyzed in Fig. 10 where a chaotic time response along with its frequency spectrum (being typically characterized by a continuous and broadband noise) and a related Poincaré section may be observed. Overall, it is noticeable that TI results and the stability analysis are consistent throughout the frequency range of interest. Where stable periodic solutions are predicted, TI and RL-HBM are superimposed. However, other types of solutions, such as solution of different periodicity, are evidenced with scattered points with TI results. In the end, this stability analysis highlights the intricacy of the nonlinear dynamic response of the system.

4.1.3 Partial conclusion

Presented results underline that considering a time-dependent gap function yields a significantly more intricate dynamics of the impactor. Indeed, in contrast to the results presented in section 3, there is a wide variety of solution types predicted by the RL-HBM when considering a time-dependent gap function. Nonetheless, it is found that the

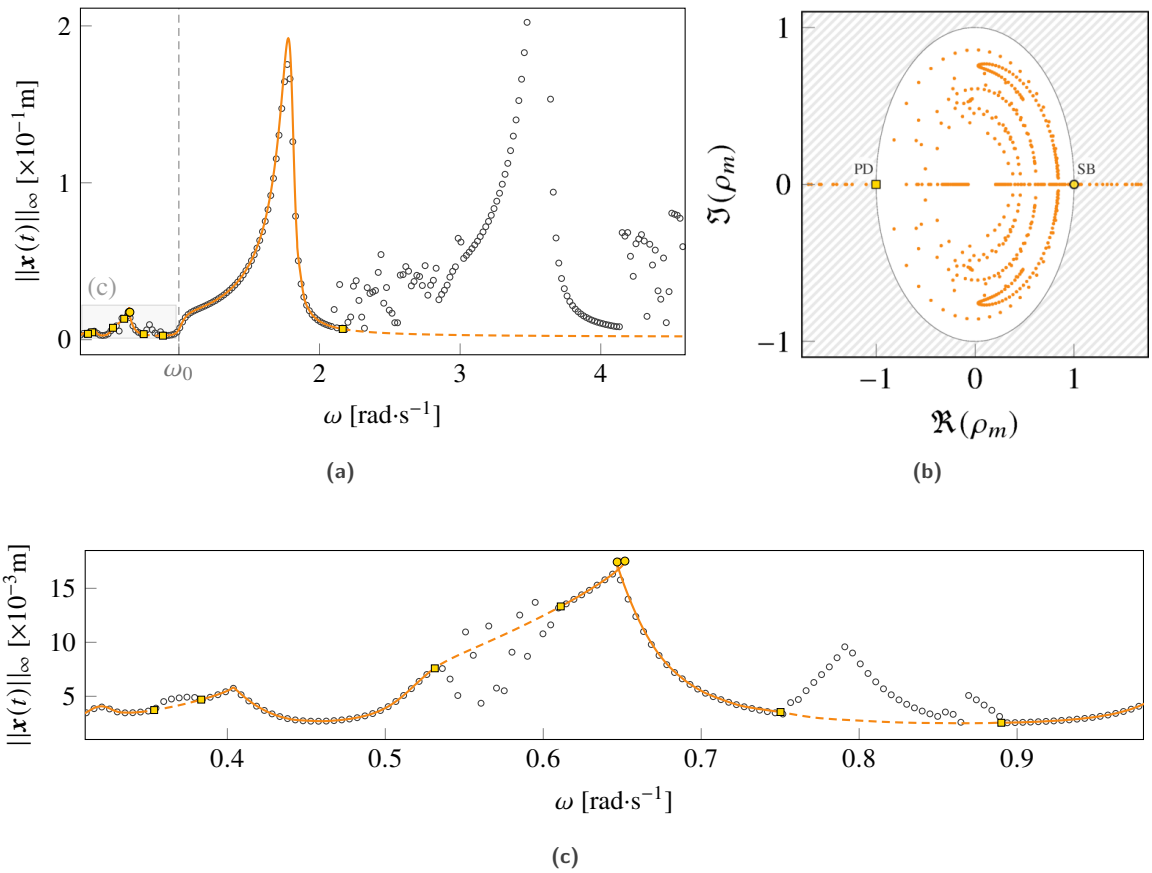

Figure 7 – (a) Nonlinear frequency response curve of the single-dof impactor (——) ($1T$-periodic branch) featuring TI results (○), corresponding (b) Floquet multipliers in the complex plane, and (c) zoom on the left of the response curve. Limit points (●) and period doubling bifurcations (■) .

RL-HBM performs very well for such system as no convergence issue was detected. The consistence between the results obtained by the Newmark $2n$-pass method and Hill's method (considering both eigenvalue and eigenvector sorting algorithms) also demonstrates the applicability of both methods in the case of contact nonlinearities. In the following, in order to avoid the issue of ambiguous coefficients, only two methods are retained for stability assessment: the Newmark $2n$-pass method and Hill's method with eigenvalue sorting. In addition, for numerical efficiency reasons, only a subset of Hill's spectrum containing $4n$ eigenvalues with lowest magnitudes is computed.

4.2 Numerical considerations for efficient computations

Blade-tip/casing interactions simulation requires a 3D contact management algorithm and to take into account several boundary nodes to represent the contact interface adequately. This increased complexity yields specific numerical challenges to ensure that the RL-HBM is numerically robust and efficient, which is essential for its potential implementation in an industrial context. While some of these challenges were previously addressed for the computation of the NFRC [22], this section presents key aspects of the methodology that have been improved further because they were identified as essential for obtaining fast and reliable stability assessment.

4.2.1 Newton solver

The Newton solver was found to be efficient despite its simplicity. Since the continuation algorithm with adaptative step control ensures (most of the time) well-chosen initial guesses, Newton's solver becomes quite performant and

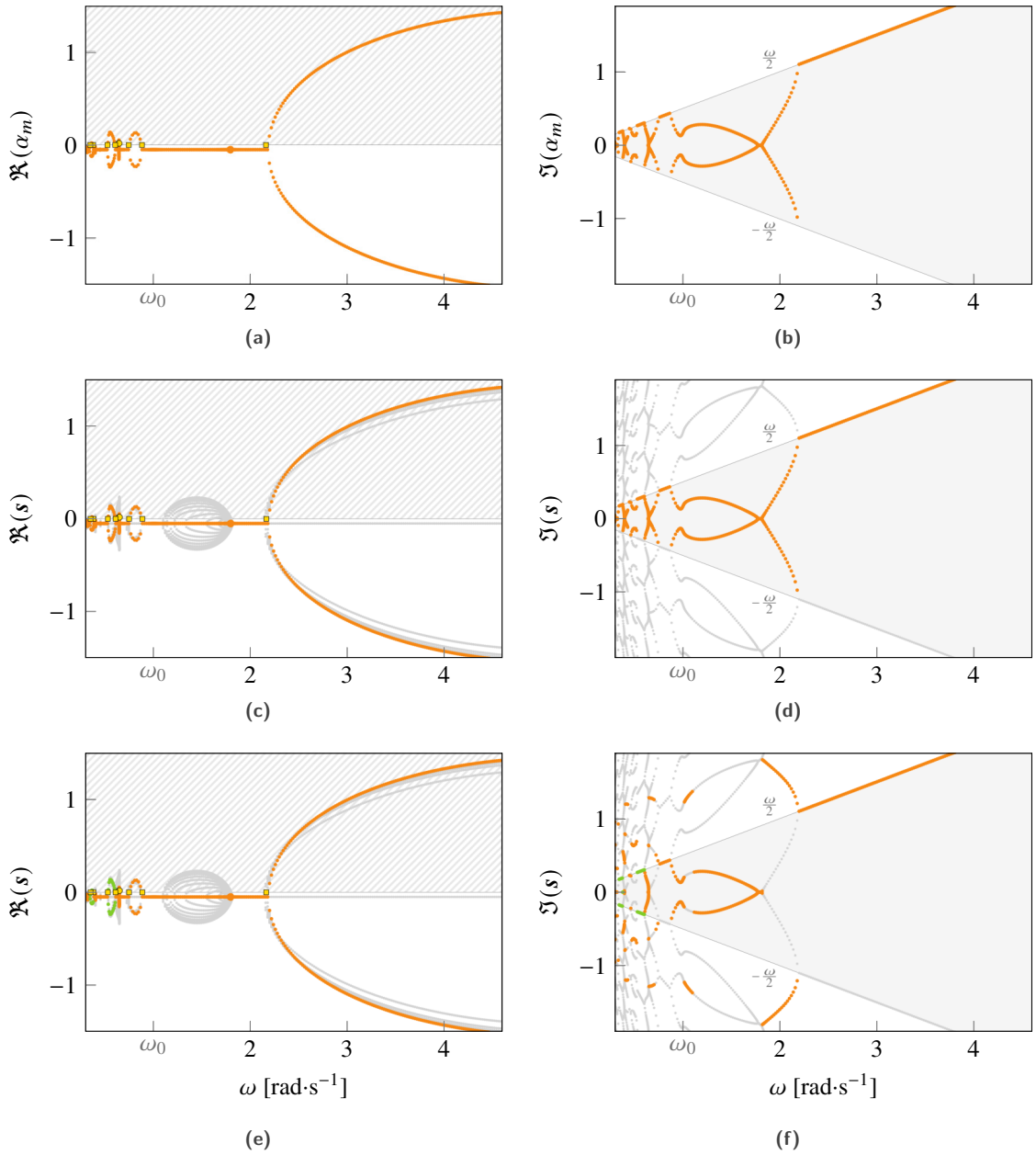

Figure 8 – Real and imaginary parts of Floquet exponents obtained with the Newmark $2n$-pass method (a)/(b) and Hill coefficients with eigenvalues (c)/(d) and eigenvectors (e)/(f) sorting algorithms. Hill coefficients (●), sorted coefficients (●) and ambiguous coefficients (●). Limit points (●) and period doubling bifurcations (■) .

demonstrates local quadratic convergence when compared to some more sophisticated numerical routines based on modified Powell's hybrid methods such as Powell's dog leg method (for instance, MINPACK subroutine HYBRD). It seems that these advanced routines may be advantageously used to initialize the solution process and thus benefit from global convergence properties for starting points far from nonlinear resonances.

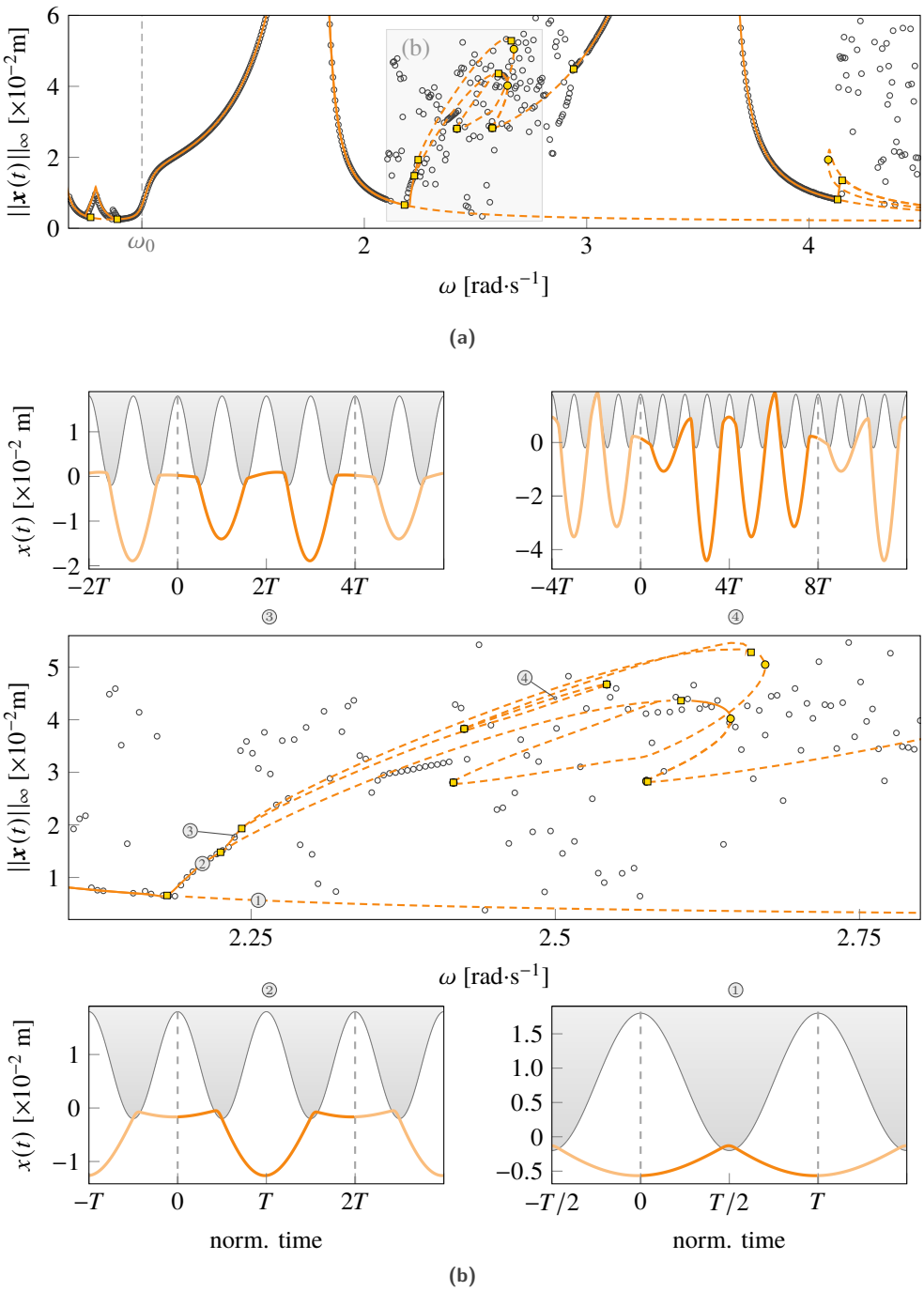

Figure 9 – Zoom on the period doubling emanating branches. Limit points (●) and period doubling bifurcations (■) . Obstacle (▭).

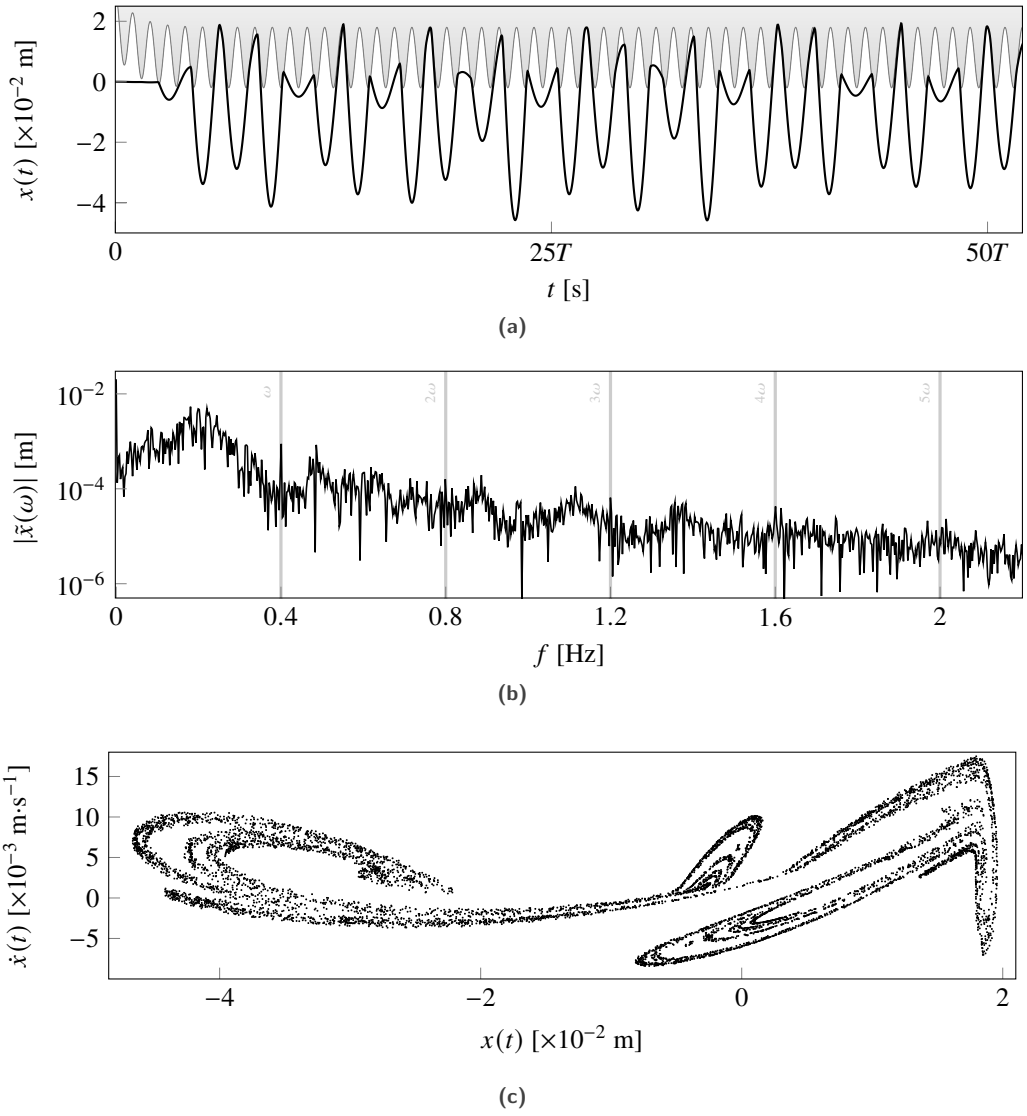

Figure 10 – Characterization of a chaotic solution obtained by TI (——) at $\omega = 2.5$ rad·s^{-1}: (a) time response, (b) associated frequency spectrum, and (c) Poincaré section. Obstacle (□).

4.2.2 Parallelized and uncoupled condensation

By taking advantage of the block diagonal structure of $\mathbf{Z}(\omega)$, the evaluation of the terms of Eq. (59) and their derivatives may be done very efficiently during the nonlinear condensation procedure. Indeed, its block diagonal structure makes it decoupled harmonic-wise. Consequently, this allows to solve individually each linear system associated to a specific harmonic block and only put back together their solutions afterwards. In fact, only the nonlinear forces eventually generate a coupling between the different harmonic blocks. It should also be noted that when there are no explicit ω dependences (*i.e.* gyroscopic or centrifugal effects) in $\mathbf{M}$, $\mathbf{C}$ and $\mathbf{K}$ matrices, the latter can be partitioned—once and for all—at the beginning of the calculation in order to construct each partitions of $\mathbf{Z}(\omega)$ more efficiently, see Eqs. (52) and (57).

4.2.3 AFT using Fast Fourier Transforms

Using Fast Fourier Transforms (FFT), as in [59] or similarly to the procedure described in [60], in the AFT procedure increases numerical performances and enhances the accuracy of the resulting frequency-domain Jacobian matrix $\partial \tilde{\boldsymbol{f}}_{\mathrm{nl}}/\partial \tilde{\boldsymbol{x}}$. In particular, real input FFT algorithms exploit the spectrum's symmetry of real-valued sequences by halving calculations by computing only their positive frequency components. The coefficients of $\partial \tilde{\boldsymbol{f}}_{\mathrm{nl}}/\partial \tilde{\boldsymbol{x}}$ may be expressed in the same fashion as in Eq. (20), as a combination of partial derivatives $\partial f_k/\partial x_l$, for $k, l \in [\![1..n]\!]$, and components of the Fourier basis $\mathcal{B}_H$ defined as:

$$\boldsymbol{\mathcal{B}}_H = \left[\frac{1}{2}, \cos(\omega t), \sin(\omega t), \ldots, \cos(H\omega t), \sin(H\omega t) \right] \tag{43}$$

and its first-order time derivative $\dot{\boldsymbol{\mathcal{B}}}_H$. For instance, the coefficient related to the partial derivative of the cosine component of the 3$^{\mathrm{rd}}$ harmonic of $\tilde{\boldsymbol{f}}_{\mathrm{nl}}$ with respect to the 2$^{\mathrm{nd}}$ harmonic sine component of the displacements $\tilde{\boldsymbol{x}}$ is:

$$\frac{\partial a_3^{\mathrm{nl},k}}{\partial b_2^l} = \frac{2}{T} \int_0^T \left[\left.\frac{\partial f_k}{\partial x_l}\right|_t \sin(2\omega t) + 2\omega \left.\frac{\partial f_k}{\partial \dot{x}_l}\right|_t \cos(2\omega t) \right] \cos(3\omega t)\, dt \tag{44}$$

Equation (44) is then approximated by forward real input FFT which yields complex Fourier coefficients that must be converted into real Fourier representation. In addition, one should note that $\mathcal{B}_H$ and $\dot{\boldsymbol{\mathcal{B}}}_H$ may be computed only once prior to computations.

4.2.4 Scaling of the problem

The numerical performances of the solver may also be improved further when considering high dimensional systems by scaling the problem (see for instance reference [61]). To this end, the equation of motion may be normalized such that Eq. (1) now reads:

$$\frac{\alpha}{\beta^2}\mathbf{M}\ddot{\boldsymbol{x}}(t) + \frac{\alpha}{\beta}\mathbf{C}\dot{\boldsymbol{x}}(t) + \alpha\mathbf{K}\boldsymbol{x}(t) + \boldsymbol{f}_{\mathrm{nl}}(\boldsymbol{x}(t), \dot{\boldsymbol{x}}(t), \omega) = \boldsymbol{f}_{\mathrm{ext}}(t, \omega) \tag{45}$$

where α and β are respectively space and time normalization factors. These factors are chosen so that $||\alpha \boldsymbol{x}|| \simeq 1$ and $\omega/\beta \simeq 1$. From there, normalization may be applied in the frequency domain by modifying the definition of $\mathbf{Z}(\omega)$ in Eq. (52), all the partial derivatives of nonlinear forces, as well as the stability Eqs. (34) and (37) accordingly. When studying blade-tip/casing interactions, α is equal to the average nominal blade-tip/casing clearance, and β corresponds to the middle of the angular velocity range of interest. In a similar fashion, to improve the quality of computed eigenvalues in Eq. (40), the quadratic eigenvalue problem (37) may be adequately scaled prior to its linearization [62].

4.3 Blade-tip/casing interactions on NASA rotor 37

Rotor 37 is a 36-blade transonic axial compressor stage that was designed at NASA's Lewis research center in the late 1970s as part of aerodynamics research [63]. It notably served as a benchmark to assess the performance of computer fluid dynamics solvers in the 1990s. More recently, a benchmark based on this blade was proposed for the analysis of blade-tip/casing contact interactions [64]. This same model was used to demonstrate the suitability of the RL-HBM [22] to predict blade-tip/casing contact related interactions.

4.3.1 Blade model

The considered finite element model of the blade is the same as the one used in some previously published works [22, 65], its main features are briefly recalled in the following. The Craig-Bampton approach is used to build a reduced-order model considering a reduction parameter $\eta = 10$. The contact interface, located at the blade-tip , contains $n_b = 8$ boundary nodes with 3 dof each evenly distributed from the leading edge to the trailing edge. The reduced model thus includes 24 nonlinear dof along with 10 modal dof therefore yielding a total of $n = 34$ dof. Convergence of the blade eigenfrequencies for the first free vibration modes with respect to the mesh size as well as to the reduction parameter η was checked but is not detailed here for the sake of brevity. The blade's structural

damping is represented by a modal damping, considering a coefficient $\xi_{1-2} = 1 \cdot 10^{-3}$ for the first bending (1B) and first torsional (1T) modes, and $\xi_{3+} = 5 \cdot 10^{-3}$ for all other modes. No inertial effects nor abradable coating wear is considered in this paper. The investigated nonlinear dynamics result essentially from pure blade-tip/casing interactions.

4.3.2 Contact scenario: deformation of the casing

First, as is usually the case for the simulation of blade-tip/casing structural contact simulations, aerodynamic forcing is here neglected as most related experimental observations were made within vacuum chambers [10]. Consequently, $\mathbf{f}_{\text{ext}}(t, \omega) = \mathbf{0}$. In addition, since experimental observations tend to indicate that the vibration amplitudes of the surrounding casing are negligible, a perfectly rigid obstacle may be considered. Finally, within an aircraft engine, blade-tip/casing contact may be initiated by a sudden acceleration of the blade—thus resulting in the application of a significant centrifugal load and a significant radial displacement of the blade-tip—or a progressive deformation of the surrounding casing due, for instance, to the application of a thermal loading. In any case, accounting for a non perfectly circular casing contact surface and typical mounting points of the casing in aircraft engines often led researchers to consider a deformed casing, usually ovalized with two privileged contact areas.

In the following, the casing is represented by a perfectly rigid mathematical profile which is assumed to be distorted in such a way that there are two symmetrical privileged contact areas along the casing circumference. Because of this distortion, contacts occur at any angular speed. In the context of the HBM, the ovalized casing translates into a T-periodic distance function in Eq. (4), its relative distance functions components $d_{j,i}$ are evaluated as follows:

$$d_{j,i} = c_j - (c_j + p_j)\,\mathrm{e}\left[-\left(\frac{(\tau_i + \theta_j) \pmod{2\pi/n_l} - \pi/n_l}{w_l}\right)^2\right] \quad \text{for} j \in [\![1..n_b]\!],\ i \in [\![0..N-1]\!] \tag{46}$$

where, n_l is the number of lobes, w_l defines the angular width of the contact areas along the casing circumference, θ_j is the angular shift of the j-th boundary node with respect to the reference position of the blade, c_j is the operating clearance and p_j defines the penetration of the casing profile with respect to the circle defined by the radial position of the j-th boundary node when the blade does not vibrate. The following values are considered in the remainder: $n_l = 2$, $w_l = 0.15$, and for all contact nodes, $c_j = 5 \cdot 10^{-4}$ m and $p_j = 1.25 \cdot 10^{-4}$ m. A cross section of the ovalized casing in front of the j-th boundary node of the blade is depicted in Fig. 11.

4.3.3 Nonlinear frequency response curve and spectral map

The blade's nonlinear response is studied at the vicinity of its linear resonance (●) corresponding to the intersection between the fourth engine order and the first bending mode of the blade ($\omega_{1\text{B}}/4$). The NFRC obtained by both TI reference strategy and RL-HBM associated to the blade's leading edge's displacement r_1 are depicted in Fig. 12. The depicted stability results are based on Hill's method. In the case of the TI reference strategy, one simulation (○) was carried every 0.25 rad·s^{-1} over 230 blade revolutions with a time step $h = 1 \cdot 10^{-7}$ s starting from null initial conditions (thus providing higher resolution results than previous publications [22]). For the RL-HBM simulations, $H = 80$, $N = 4096$ and a unitary ($m = C_H = 1$) Lanczos filter are considered. Normal contact forces are computed with the regularized penalty law given in Eq. (7) with $\kappa = 1 \cdot 10^9$ N·m^{-1} and $\gamma = 6 \cdot 10^2$ N. For both methodologies, dry friction forces are accounted for with $\mu = 0.15$.

One should emphasize that RL-HBM and TI reference strategy fundamentally differ both in terms of solution paradigm and contact treatment (regularized penalty law *vs.* Lagrange multipliers). Nonetheless an excellent agreement between the two methodologies is observed. A small area of discrepancy may be seen at 1535 rad·s^{-1} which is due to the difference of contact laws. Also, the area of higher disparity, see Fig. 12c, is explained in the remainder thanks to the stability analysis.

Limit points (●) are localized around the two folds of the NFRC, namely about $\omega = 1410$ rad·s^{-1}, see Fig. 12b, and along the nonlinear primary resonance. In addition, Neimark-Sacker bifurcations (▲) enclose a zone of high disparity between TI and RL-HBM for which TI solutions are characterized by a richer frequency content, see Fig. 12c. The stability analysis therefore allows to accurately pinpoint a zone where potentially higher amplitude solutions could be detected by TI. From an industrial perspective, these results enable to advantageously focus the

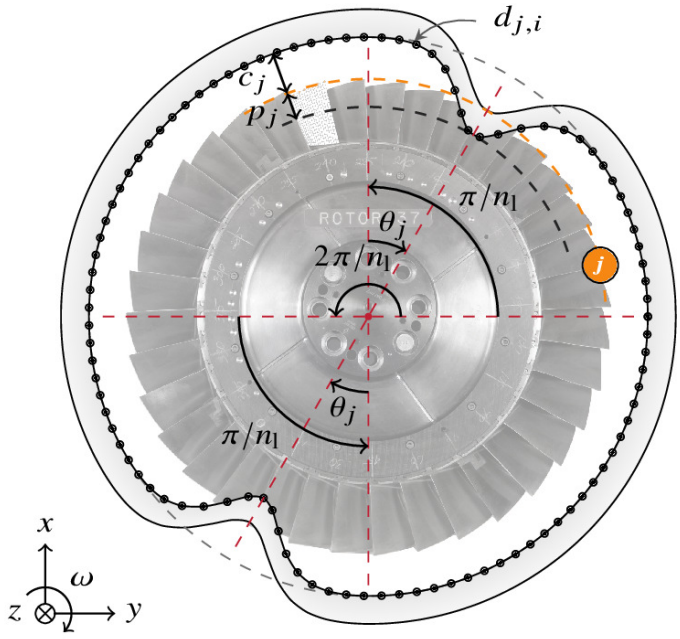

Figure 11 – Deformed casing (□) with respect to the j-th boundary node (●) of the rotor 37 blade [66].

integrator on specific angular velocity range associated to potentially sensitive areas of the NFRC. The relevance of the filtering procedure is underlined here as it is evidenced that the total number of solutions required to computed the NFRC is significantly decreased: 20 % less solutions are required to depict the NFRC of the blade ($m = 1$) when filtering is considered. Thus providing significant improvements in terms of computational cost and improving the overall convergence of the iterative solver.

The real parts of the corresponding Floquet exponents that led to these results, from both time and frequency-domain methodologies, are now exposed in Fig. 13. The vast majority of the predicted Floquet exponents and multipliers do not agree well between the two algorithms. Indeed, a good agreement between the stability coefficients obtained with Newmark $2n$-pass algorithm and Hill's method is found for larger real part values. Indeed, as it was already underlined in an other study [26], for complex structures, it seems that the theoretical relations between the Floquet exponents, Hill coefficients (unsorted spectrum), and the excitation frequency ω, see Eq. (41), may not be applied as the distribution of Hill coefficients in the complex plane is rather intricate and this inevitably leads to a partly accurate sorting. Nevertheless, a qualitative stability assessment still appears to be achievable, as shown in Fig. 12.

Convergence of stability results is depicted in Fig. 14. In Fig. 14a, the real parts of the Floquet exponents obtained for $H = \{40(●), 60(●), 80(●)\}$ with $N = 2048$, and for $H, N = \{80, 4096\}$ (●) are pictured. In Fig. 14b, the real parts of the selected Hill coefficients that were obtained for $H = \{40(●), 60(●), 80(●)\}$ with $N = 2048$, and for $H, N = \{80, 4096\}$ (●) are represented. Overall, the Newmark $2n$-pass algorithm is slower to converge than Hill's method to a point where even for a well-converged NFRC in terms of displacements it still yields an erroneous stability verdict. This was unexpected as previous studies [32] tend to suggest otherwise.

Looking at the leading Floquet exponent, results obtained with the Newmark $2n$-pass method seem to asymptotically converge towards results obtained with Hill's method as the number of harmonics H and time samples per period N are increased. While the displacements NFRC could accurately be computed using an AFT procedure with a relatively low number of samples ($N = 1024$), severe contact configurations (for $\gamma \to 0$ regularization values) may even require a larger harmonics content and higher number of time samples in order to get converged stability results. From a numerical perspective, it should been underlined that low degree of smoothness nonlinearities still

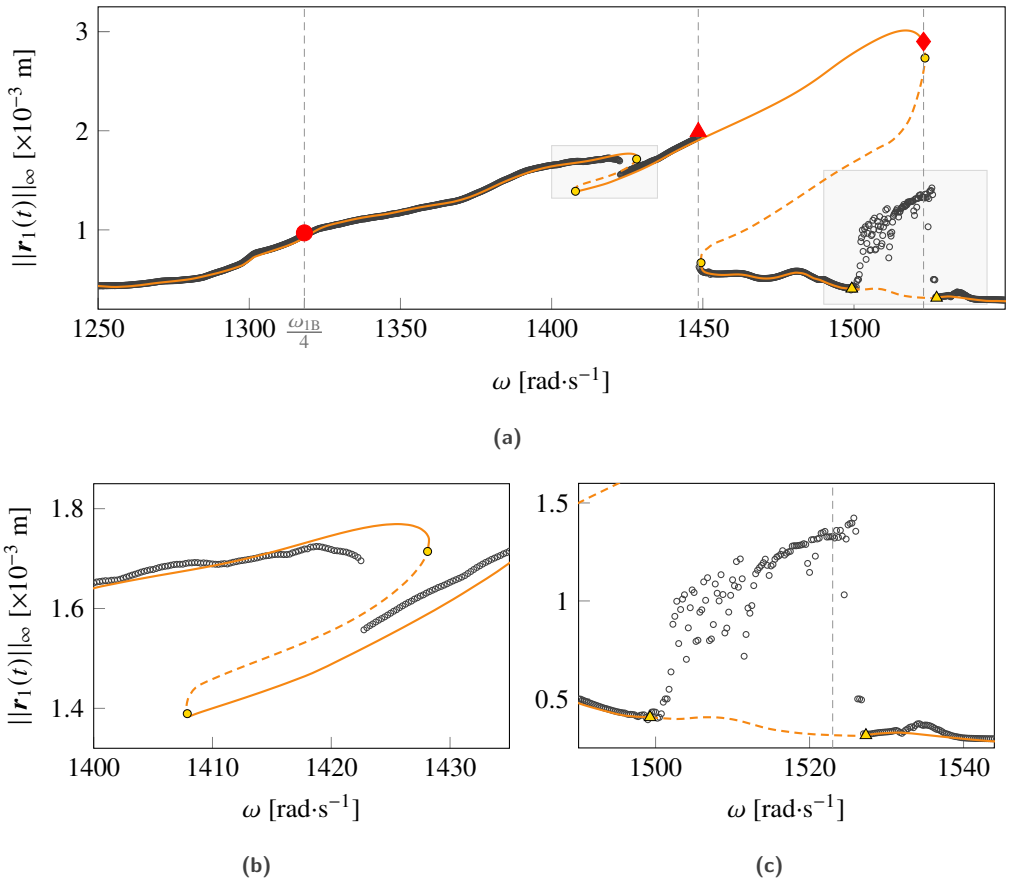

Figure 12 – Rotor 37 blade numerical results: (a) nonlinear frequency response curve, (b) zoom on the fold and (c) high disparity areas. Limit points (●) and Neimark-Sacker bifurcations (▲) .

constitute a major challenge for both time and frequency-domain stability analysis algorithms.

4.3.4 Influence of filtering over stability assessment

The influence of Lanczos filtering over the resulting stability analysis is here addressed. First, the critical Floquet multiplier corresponding to the one having the highest magnitude for a given solution is defined as:

$$\rho_{\text{crit}} = \underset{m \in [\![1\,..\,2n]\!]}{\arg\max} |\rho_m| \tag{47}$$

The investigation is focused solely on the smoothing exponent m used to define the Lanczos factors σ_j in Eq. (23) as the cut-off harmonic requires an *a priori* knowledge on the nature of the nonlinearity to be efficiently tuned which is goes beyond the scope of this paper. The smoothing parameter is critical in that it controls the intensity of filtering, it is therefore necessary to quantify its impact over the resulting stability analysis. To this end, several NFRC of the blade are computed using various filtering exponents $m = \{0(\text{——}), 0.5(\text{——}), 1(\text{——}), 1.5(\text{——}), 2(\text{——})\}$ for $H, N = \{80, 4096\}$ and magnitudes of their corresponding critical Floquet multipliers as a function of the angular velocity is depicted in Fig. 15.

Filtering appears to have an almost negligible influence over the stability verdict resulting from Hill's method on complex systems. Indeed, increasing m solely causes a slight angular velocity shift on the resulting NFRC without inducing significant uncertainties in the stability analysis as depicted in Fig. 16. Limit points are still predicted in the vicinity of the vertical tangents and the slight variation on the localizations of Neimark-Sacker bifurcations is

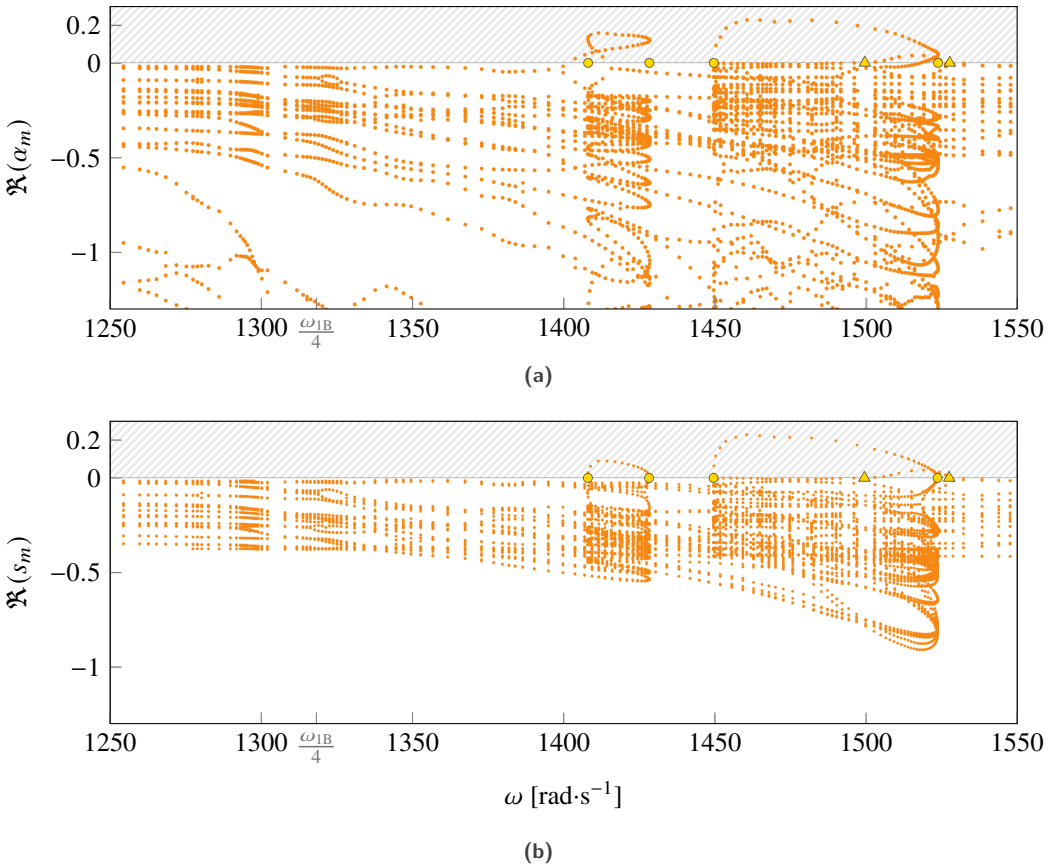

Figure 13 – Real parts of Floquet exponents (●) obtained with the Newmark $2n$-pass method (a) and Hill's method with eigenvalue sorting (b). Limit points (●) and Neimark-Sacker bifurcations (△) .

mainly due to the different discretizations of the solutions along the NFRC.

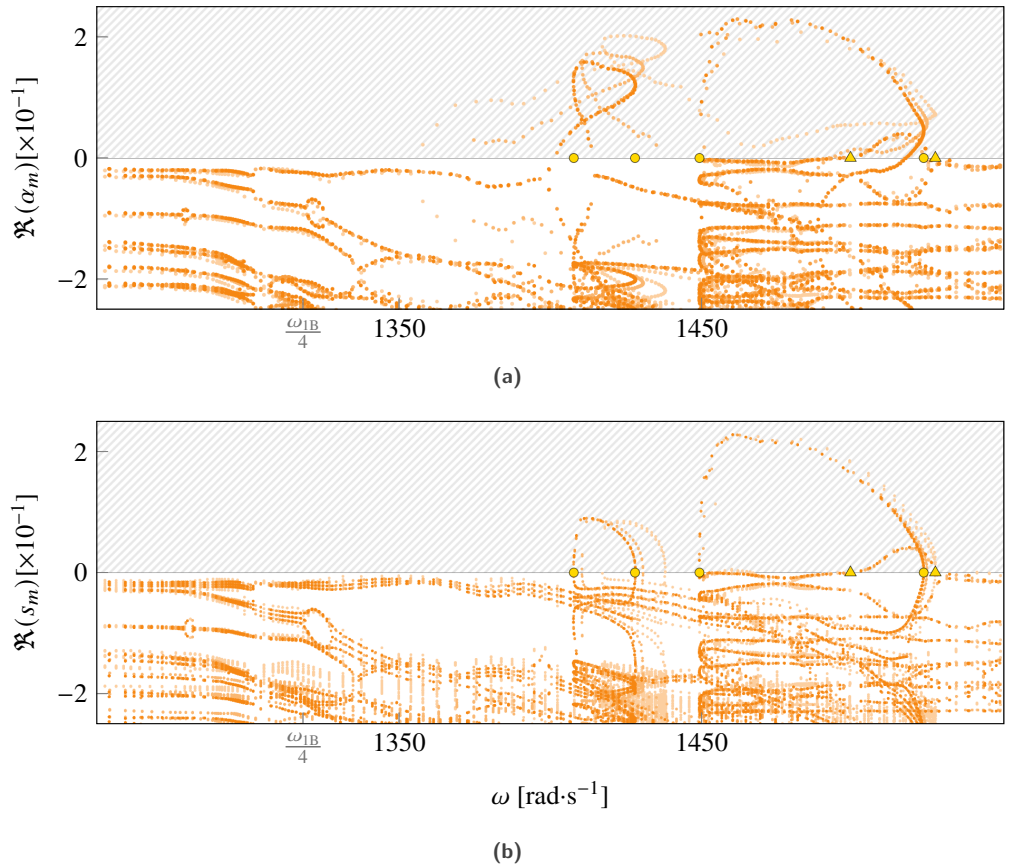

Figure 14 – Convergence of the real parts of Floquet exponents obtained with the Newmark $2n$-pass method (a) and Hill's method with eigenvalue sorting (b). Stability coefficients obtained for $H = \{40(\bullet), 60(\bullet), 80(\bullet)\}$ with $N = 2048$, and for $H, N = \{80, 4096\}$ ($\bullet$). Limit points ($\bullet$) and Neimark-Sacker bifurcations ($\blacktriangle$) .

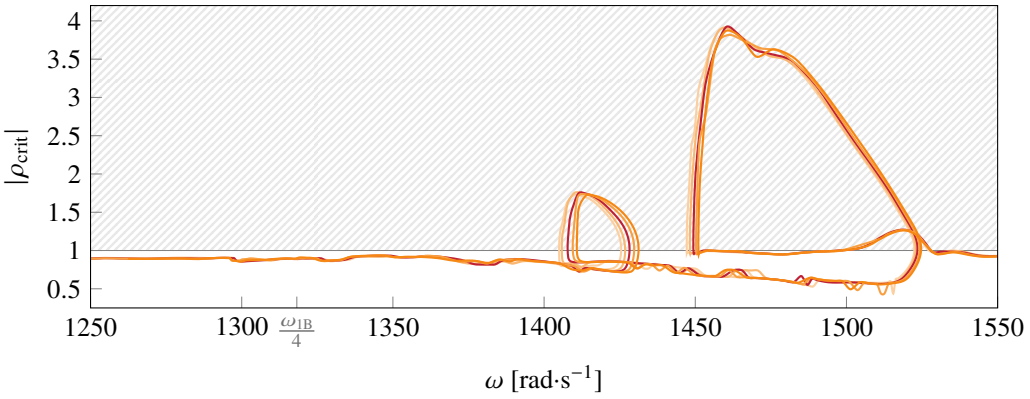

Figure 15 – Influence of filtering exponent m over the modulus of the leading Floquet multiplier ρ_{crit}. Filtering exponents values $m = \{0(\text{——}), 0.5(\text{——}), 1(\text{——}), 1.5(\text{——}), 2(\text{——})\}$ for $H, N = \{80, 4096\}$.

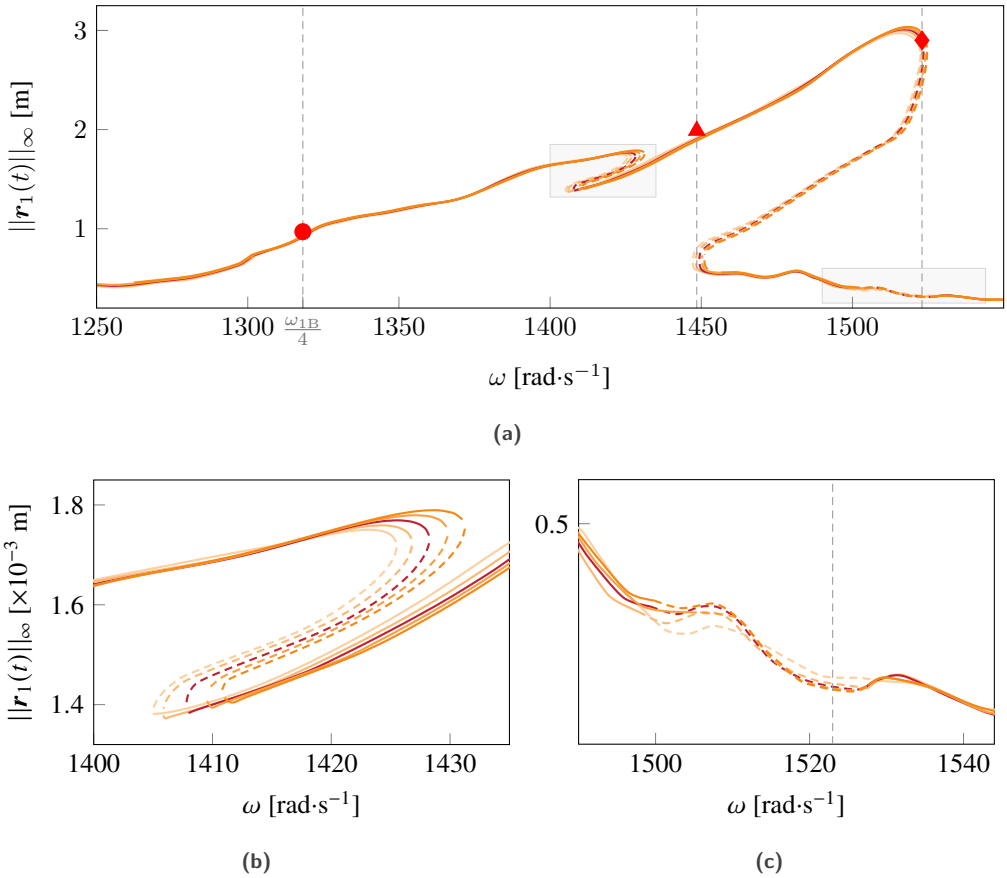

Figure 16 – (a) Influence of filtering exponent m, zoom on the (b) fold and (c) high disparity areas. Filtering exponents values $m = \{0(\text{——}), 0.5(\text{——}), 1(\text{——}), 1.5(\text{——}), 2(\text{——})\}$ for $H, N = \{80, 4096\}$.

5 Conclusion

In this article, the assessment of the local stability of periodic solutions computed for various mechanical systems subjected to unilateral contact constraints—including an industrial reduced order model of a blade subjected to repeated contact interactions with its surrounding casing—is investigated. All periodic solutions are computed with a previously introduced harmonic balance method-based numerical approach featuring a regularization of the contact law and a Lanczos filtering procedure of nonlinear contact forces. For single-degree of freedom impactors, it is shown that an appropriate eigenvalue sorting of Hill coefficients is key to properly select the related Floquet exponents in the presence of period doubling bifurcations. Stability assessment is also shown to be more numerically sensitive in the presence of time-dependent gap configurations as such configuration yields a significantly increased complexity of the system's dynamics. Finally, the stability analysis of periodic solutions related to blade-tip/casing interactions obtained with RL-HBM is performed. Presented results indicate that Hill's method is better suited for the evaluation of the stability of solutions resulting from an harmonic balance solver than the Newmark $2n$-pass method for which a slower convergence is underlined. The influence of filtering appears to be negligible over the resulting stability assessment thus making the use of filtering fully compatible with a stability assessment of the resulting periodic solutions of industrial blades. These findings pave the way of the qualitative understanding of such interactions and complement the results offered by a well-established quantitative industrial time integration strategy.

Acknowledgment

This research was supported by the Canada Research Chairs Program (Funder ID: 10.13039/501100001804).

A Computation of nonlinear forced response curves using the Harmonic Balance Method

Although already well-described in a previous publication [22], the fundamentals of the harmonic balance based numerical approach used in this article are recalled here for the sake of completeness.

HBM framework relies on the assumption that the solutions of Eq. (1) $\boldsymbol{x}$ may be expressed as H-truncated Fourier series:

$$\boldsymbol{x}(t) \simeq \frac{1}{2}\boldsymbol{a}_0 + \sum_{j=1}^{H} \left[\boldsymbol{a}_j \cos\left(j\omega t\right) + \boldsymbol{b}_j \sin\left(j\omega t\right)\right] \tag{48}$$

By applying the same spectral decomposition to nonlinear and external forces, respectively $\boldsymbol{f}_{\text{nl}}$ and $\boldsymbol{f}_{\text{ext}}$, the $n(2H+1)$ Fourier coefficients belonging to each quantity may then be gathered accordingly within the related frequency domain vectors identified by the symbol $(\sim)$. For instance, Fourier coefficients of nonlinear forces take the following form:

$$\tilde{\boldsymbol{f}}_{\text{nl}} = \left[\, \boldsymbol{a}_0^{\text{nl}},\, \boldsymbol{a}_1^{\text{nl}},\, \boldsymbol{b}_1^{\text{nl}},\, \ldots,\, \boldsymbol{a}_H^{\text{nl}},\, \boldsymbol{b}_H^{\text{nl}} \,\right]^\top \tag{49}$$

where vectorial quantities $\boldsymbol{a}_j^{\text{nl}}$ are the unknown real Fourier coefficients respectively related to cosine terms and $\boldsymbol{b}_j^{\text{nl}}$ the ones related to sine terms. Each of these coefficients are defined as follows:

$$\begin{cases} \boldsymbol{a}_j^{\text{nl}} = \left[a_j^{\text{nl},1},\, a_j^{\text{nl},2},\, \ldots,\, a_j^{\text{nl},n}\right] & \text{for } j \in [\![0..H]\!] \\ \boldsymbol{b}_j^{\text{nl}} = \left[b_j^{\text{nl},1},\, b_j^{\text{nl},2},\, \ldots,\, b_j^{\text{nl},n}\right] & \text{for } j \in [\![1..H]\!] \end{cases} \tag{50}$$

From that point, Fourier approximations of displacement vector $\boldsymbol{x}(t)$ of Eq. (48), its time derivatives, $\dot{\boldsymbol{x}}(t)$ and $\ddot{\boldsymbol{x}}(t)$, along with forces, are substituted into the equation of motion, following which a Fourier-Galerkin projection is applied to transform the initial nonlinear differential system of dimension n into $n(2H+1)$ nonlinear algebraic equations in the frequency domain:

$$\mathbf{R}(\tilde{\boldsymbol{x}}, \omega) = \mathbf{Z}(\omega)\tilde{\boldsymbol{x}} + \tilde{\boldsymbol{f}}_{\text{nl}}(\tilde{\boldsymbol{x}}, \omega) - \tilde{\boldsymbol{f}}_{\text{ext}}(\omega) = \mathbf{0} \tag{51}$$

where $\mathbf{Z}(\omega)$ is the block diagonal dynamic stiffness matrix which characterizes the linear dynamics of the response of the system. It is defined as follows:

$$\mathbf{Z}(\omega) = \omega^2 \boldsymbol{\nabla}^2 \otimes \mathbf{M} + \omega \boldsymbol{\nabla} \otimes \mathbf{C} + \mathbf{I}_{2H+1} \otimes \mathbf{K} \tag{52}$$

where $\otimes$ stands for the Kronecker product and $\mathbf{I}_{2H+1}$ is the identity matrix of size $2H+1$. The matrix $\boldsymbol{\nabla}$ corresponds to a frequency-domain differential operator and is given by:

$$\boldsymbol{\nabla} = \text{diagblock}(0,\ \boldsymbol{\nabla}_1,\ \ldots,\ \boldsymbol{\nabla}_j,\ \ldots,\ \boldsymbol{\nabla}_H) \quad \text{and} \quad \boldsymbol{\nabla}^2 = \boldsymbol{\nabla}\boldsymbol{\nabla} \tag{53}$$

with the elementary first order derivative matrix $\boldsymbol{\nabla}_j$:

$$\boldsymbol{\nabla}_j = j \begin{bmatrix} 0 & 1 \\ -1 & 0 \end{bmatrix} \text{ for } j \in [\![1..H]\!] \tag{54}$$

A Newton-Raphson algorithm may then be used in order to search for solutions of Eq. (51). Starting from a proper initial guess $\tilde{\boldsymbol{x}}^0$, a converged solution is obtained iteratively:

$$\tilde{\boldsymbol{x}}^{k+1} = \tilde{\boldsymbol{x}}^k + \Delta\tilde{\boldsymbol{x}}^k \quad \text{with} \quad \mathbf{R}^k_{,\tilde{\boldsymbol{x}}} \Delta\tilde{\boldsymbol{x}}^k = -\mathbf{R}^k \tag{55}$$

where $\mathbf{R}^k = \mathbf{R}(\tilde{\boldsymbol{x}}^k, \omega)$ is the residual at iteration k and $\mathbf{R}^k_{,\tilde{\boldsymbol{x}}}$ is the Jacobian matrix of the system with respect to $\tilde{\boldsymbol{x}}^k$:

$$\mathbf{R}^k_{,\tilde{\boldsymbol{x}}} = \frac{\partial \mathbf{R}}{\partial \tilde{\boldsymbol{x}}}(\tilde{\boldsymbol{x}}^k, \omega) = \mathbf{Z}(\omega) + \tilde{\boldsymbol{f}}_{\text{nl},\tilde{\boldsymbol{x}}} = \mathbf{Z}(\omega) + \frac{\partial \tilde{\boldsymbol{f}}_{\text{nl}}(\tilde{\boldsymbol{x}}^k, \omega)}{\partial \tilde{\boldsymbol{x}}} \tag{56}$$

Newton's corrections cycle ends once a relative error convergence criterion is met.

Continuation techniques are usually coupled to the HBM solver. These techniques either fall into predictor/corrector type of methods or the asymptotic numerical method, and it has been shown that the former are more appropriate for dealing with nonsmooth nonlinearities such as structural contact [67]. As a result, in this paper, a predictor/corrector strategy where Newton's search direction is constrained by an additional arc-length parameterization scalar equation is used. This advantageously allows (1) to compute a continuum of solutions, *i.e.* a branch of solutions, instead of discrete solutions for each considered angular velocities ω therefore increasing the qualitative contribution of such an approach within a nonlinear context, and (2) to feed adequate initial guess to Newton's solver thus increasing its numerical robustness and efficiency. In this paper, and as in [22], predictions are obtained by means of a secant predictor which has been found to be more robust than the tangent predictor when dealing with contact nonlinearities.

Alternating Frequency/Time scheme (AFT) [68] is used to evaluate the nonlinear contact forces and their derivatives in the frequency domain. As there is no explicit analytical expression to directly evaluate these quantities in Fourier domain, AFT relies on using back and forth inverse and forward Discrete Fourier Transforms (DFT) to switch between the time and frequency-domain representations of the quantities of interest. At the k-th Newton iteration, starting from the multiharmonic vector of the displacements in Fourier domain $\tilde{\boldsymbol{x}}$, an inverse DFT is performed to compute the related displacements and velocities in time domain. The expression of nonlinear forces $\boldsymbol{f}_{\text{nl}}(\boldsymbol{x}, \dot{\boldsymbol{x}}, \omega)$ and their partial derivatives $\boldsymbol{f}_{\text{nl},\boldsymbol{x}}$, $\boldsymbol{f}_{\text{nl},\dot{\boldsymbol{x}}}$ and $\boldsymbol{f}_{\text{nl},\omega}$ are then evaluated. These terms are then translated back into the frequency domain using a forward DFT to obtain their frequency-domain counterparts $\tilde{\boldsymbol{f}}_{\text{nl}}$, $\tilde{\boldsymbol{f}}_{\text{nl},\tilde{\boldsymbol{x}}}$ and $\tilde{\boldsymbol{f}}_{\text{nl},\omega}$. Semi-analytical derivatives may be obtained in the frequency domain thanks to the linearity property of the DFT operators and the chain rule, see [22, 1]. Newton's correction is then computed and applied to $\tilde{\boldsymbol{x}}^k$ which corresponds to Eq. (55). From that point, if the convergence criterion has not been satisfied, a new cycle of AFT begins.

Nonlinear dof condensation is one of the key numerical perk of the HBM when dealing with systems featuring localized nonlinearities like the ones resulting from blade-tip/casing interactions. It is based on a reorganization of Eq. (51). This reorganization relies on a partition of the dof into nonlinear *vs.* linear dof, *i.e.* dof that are involved, or not, in the computation of nonlinear forces $\boldsymbol{f}_{\text{nl}}(\boldsymbol{x}, \dot{\boldsymbol{x}}, \omega)$, so that Eq. (51) which may then be expressed as:

$$\begin{bmatrix} \mathbf{Z}^{\text{ll}} & \mathbf{Z}^{\text{lnl}} \\ \mathbf{Z}^{\text{nll}} & \mathbf{Z}^{\text{nlnl}} \end{bmatrix} \begin{bmatrix} \tilde{\boldsymbol{x}}^{\text{l}} \\ \tilde{\boldsymbol{x}}^{\text{nl}} \end{bmatrix} + \begin{bmatrix} \tilde{\boldsymbol{f}}^{\text{l}}_{\text{nl}}(\tilde{\boldsymbol{x}}^{\text{nl}}) \\ \tilde{\boldsymbol{f}}^{\text{nl}}_{\text{nl}}(\tilde{\boldsymbol{x}}^{\text{nl}}) \end{bmatrix} - \begin{bmatrix} \tilde{\boldsymbol{f}}^{\text{l}}_{\text{ext}} \\ \tilde{\boldsymbol{f}}^{\text{nl}}_{\text{ext}} \end{bmatrix} = \mathbf{0} \tag{57}$$

The first line of Eq. (57) leads to the expression of the linear dof $\tilde{\boldsymbol{x}}^{\mathrm{l}}$ as a function of the nonlinear dof $\tilde{\boldsymbol{x}}^{\mathrm{nl}}$:

$$\tilde{\boldsymbol{x}}^{\mathrm{l}} = \mathbf{Z}^{\mathrm{ll}^{-1}} \left[\tilde{\boldsymbol{f}}^{\mathrm{l}}_{\mathrm{ext}} - \mathbf{Z}^{\mathrm{lnl}} \tilde{\boldsymbol{x}}^{\mathrm{nl}} - \tilde{\boldsymbol{f}}^{\mathrm{l}}_{\mathrm{nl}} \left(\tilde{\boldsymbol{x}}^{\mathrm{nl}} \right) \right] \tag{58}$$

which may be used in the second line of Eq. (57) to reduce the dimension of the system to that of the nonlinear dof $\tilde{\boldsymbol{x}}^{\mathrm{nl}}$:

$$\left[\mathbf{Z}^{\mathrm{nlnl}} - \mathbf{Z}^{\mathrm{nll}} \mathbf{Z}^{\mathrm{ll}^{-1}} \mathbf{Z}^{\mathrm{lnl}} \right] \tilde{\boldsymbol{x}}^{\mathrm{nl}} + \left(\tilde{\boldsymbol{f}}^{\mathrm{nl}}_{\mathrm{nl}} (\tilde{\boldsymbol{x}}^{\mathrm{nl}}) - \mathbf{Z}^{\mathrm{nll}} \mathbf{Z}^{\mathrm{ll}^{-1}} \tilde{\boldsymbol{f}}^{\mathrm{l}}_{\mathrm{nl}} \left(\tilde{\boldsymbol{x}}^{\mathrm{nl}} \right) \right) - \left(\tilde{\boldsymbol{f}}^{\mathrm{nl}}_{\mathrm{ext}} - \mathbf{Z}^{\mathrm{nll}} \mathbf{Z}^{\mathrm{ll}^{-1}} \tilde{\boldsymbol{f}}^{\mathrm{l}}_{\mathrm{ext}} \right) = \mathbf{0} \tag{59}$$

Once a converged solution to Eq. (59) is found, the response related to the linear dof $\tilde{\boldsymbol{x}}^{\mathrm{l}}$ is computed straightforwardly by evaluating Eq. (58). More details about these reduction techniques can be found in references [22, 6, 69].

References

[1] Krack, M., Salles, L., and Thouverez, F., 2017. "Vibration prediction of bladed disks coupled by friction joints". *Arch. Comput. Methods Eng.,* **24**(3), pp. 589–636. doi : 10.1007/s11831-016-9183-2 - oai: hal-01825517.

[2] Jacquet-Richardet, G., Torkhani, M., Cartraud, P., Thouverez, F., Baranger, T. N., Herran, M., Gibert, C., Baguet, S., Almeida, P., and Peletan, L., 2013. "Rotor to stator contacts in turbomachines. Review and application". *Mech. Syst. Sig. Process.,* **40**(2), pp. 401–420. doi : 10.1016/j.ymssp.2013.05.010 - oai: hal-00934050.

[3] Kim, Y. B., Noah, S. T., and Choi, Y. S., 1991. "Periodic response of multi-disk rotors with bearing clearances". *J. Sound Vib.,* **144**(3), pp. 381–395. doi : 10.1016/0022-460X(91)90558-2 - oai: hal-01693096.

[4] Panning, L., Sextro, W., and Popp, K., 2000. "Optimization of interblade friction damper design". In Proceedings of the ASME Turbo Expo 2000, p. 8. doi : 10.1115/2000-GT-0541.

[5] Siewert, C., Panning, L., Wallaschek, J., and Richter, C., 2010. "Multiharmonic forced response analysis of a turbine blading coupled by nonlinear contact forces". *J. Eng. Gas Turbines Power,* **132**(8). doi: 10.1115/1.4000266.

[6] Petrov, E. P., 2011. "A High-Accuracy Model Reduction for Analysis of Nonlinear Vibrations in Structures With Contact Interfaces". *J. Eng. Gas Turbines Power,* **133**(10), p. 10. doi : 10.1115/1.4002810.

[7] Krack, M., Panning-von Scheidt, L., and Wallaschek, J., 2016. "On the interaction of multiple traveling wave modes in the flutter vibrations of friction-damped tuned bladed disks". *J. Eng. Gas Turbines Power,* **139**(4), p. 9. doi : 10.1115/1.4034650.

[8] Almeida, P., Gibert, C., Thouverez, F., Leblanc, X., and Ousty, J.-P., 2016. "Numerical analysis of bladed disk–casing contact with friction and wear". *J. Eng. Gas Turbines Power,* **138**(12), p. 11. doi : 10.1115/1.4033065.

[9] Padova, C., Barton, J., Dunn, M. G., and Manwaring, S., 2006. "Experimental results from controlled blade tip/shroud rubs at engine speed". *J. Turbomach.,* **129**(4), pp. 713–723. doi : 10.1115/1.2720869 - oai: hal-01333702v1.

[10] Millecamps, A., Brunel, J.-F., Dufrénoy, P., Garcin, F., and Nucci, M., 2009. "Influence of thermal effects during blade-casing contact experiments". In Proceedings of the ASME IDETC/CIE 2009, pp. 855–862. doi : 10.1115/DETC2009-86842 - oai: hal-01223060.

[11] Almeida, P., Gibert, C., Thouverez, F., Leblanc, X., and Ousty, J.-P., 2015. "Experimental analysis of dynamic interaction between a centrifugal compressor and its casing". *J. Turbomach.,* **137**(3), p. 031008. doi : 10.1115/1.4028328 - oai: hal-01574149.

[12] Zhang, B., and Marshall, M., 2019. "Investigating material removal mechanism of al-si base abradable coating in labyrinth seal system". *Wear,* **426-427**, pp. 239–249. doi : 10.1016/j.wear.2019.01.034.

[13] Nyssen, F., Tableau, N., Lavazec, D., and Batailly, A., 2020. "Experimental and numerical characterization of a ceramic matrix composite shroud segment under impact loading". *J. Sound Vib.,* **467**, p. 115040. doi : 10.1016/j.jsv.2019.115040 - oai: hal-02378746.

[14] Childs, D. W., 1976. "A modal transient rotordynamic model for dual-rotor jet engine systems". *J. Eng. Ind.,* **98**(3), pp. 876–882. doi : 10.1115/1.3439046.

[15] Black, H. F., 1968. "Interaction of a whirling rotor with a vibrating stator across a clearance annulus". *J. Mech. Eng. Sci.,* **10**(1), pp. 1–12. doi : 10.1243/JMES_JOUR_1968_010_003_02.

[16] Jiang, J., 2007. "The analytical solution and the existence condition of dry friction backward whirl in rotor-to-stator contact systems". *J. Vib. Acoust.,* **129**(2), pp. 260–264. doi : 10.1115/1.2345677.

[17] Von Groll, G., and Ewins, D. J., 2001. "The harmonic balance method with arc-length continuation in rotor/stator contact problems". *J. Sound Vib.,* **241**(2), pp. 223–233. doi : 10.1006/jsvi.2000.3298 - oai: hal-01333704.

[18] Peletan, L., Baguet, S., Torkhani, M., and Jacquet-Richardet, G., 2014. "Quasi-periodic harmonic balance method for rubbing self-induced vibrations in rotor–stator dynamics". *Nonlinear Dyn.,* **78**(4), pp. 2501–2515. doi : 10.1007/s11071-014-1606-8 - oai: hal-01061265.

[19] Xie, L., Baguet, S., Prabel, B., and Dufour, R., 2017. "Bifurcation tracking by Harmonic Balance Method for performance tuning of nonlinear dynamical systems". *Mech. Syst. Sig. Process.,* **88**, pp. 445–461. doi : 10.1016/j.ymssp.2016.09.037 - oai: hal-01402109.

[20] Alcorta, R., 2021. "Prediction of non-linear responses and bifurcations of impacting systems : Contribution to the understanding of steam generator vibrations". PhD thesis, INSA de Lyon. doi: tel-03406785.

[21] Batailly, A., Legrand, M., Millecamps, A., and Garcin, F., 2015. "Conjectural bifurcation analysis of the contact-induced vibratory response of an aircraft engine blade". *J. Sound Vib.,* **348**, pp. 239–262. doi : 10.1016/j.jsv.2015.03.005 - oai: hal-01223575.

[22] Colaïtis, Y., and Batailly, A., 2021. "The harmonic balance method with arc-length continuation in blade-tip/casing contact problems". *J. Sound Vib.,* **502**, p. 116070. doi : 10.1016/j.jsv.2021.116070 - oai: hal-03163560.

[23] Lesaffre, N., Sinou, J.-J., and Thouverez, F., 2007. "Contact analysis of a flexible bladed-rotor". *Eur. J. Mech. A/Solids,* **26**(3), pp. 541–557. doi : 10.1016/j.euromechsol.2006.11.002 - oai: hal-00322887.

[24] Petrov, E. P., 2012. "Multiharmonic analysis of nonlinear whole engine dynamics with bladed disc-casing rubbing contacts". In Proceedings of the ASME Turbo Expo 2012, pp. 1181–1191. doi: 10.1115/GT2012-68474.

[25] Salles, L., Staples, B., Hoffmann, N., and Schwingshackl, C., 2016. "Continuation techniques for analysis of whole aeroengine dynamics with imperfect bifurcations and isolated solutions". *Nonlinear Dyn.,* **86**, pp. 1897–1911. doi : 10.1007/s11071-016-3003-y.

[26] Petrov, E. P., 2017. "Stability Analysis of Multiharmonic Nonlinear Vibrations for Large Models of Gas Turbine Engine Structures With Friction and Gaps". *J. Eng. Gas Turbines Power,* **139**(2), p. 022508. doi: 10.1115/1.4034353.

[27] Petrov, E. P., 2018. "A Method for Parametric Analysis of Stability Boundaries for Nonlinear Periodic Vibrations of Structures With Contact Interfaces". *J. Eng. Gas Turbines Power,* **141**(3), p. 11. doi : 10.1115/1.4040850.

[28] Batailly, A., Agrapart, Q., Millecamps, A., and Brunel, J.-F., 2016. "Experimental and numerical simulation of a rotor/stator interaction event localized on a single blade within an industrial high-pressure compressor". *J. Sound Vib.,* **375**, pp. 308–331. doi : 10.1016/j.jsv.2016.03.016 - oai: hal-01342401.

[29] Carpenter, N. J., Taylor, R. L., and Katona, M. G., 1991. "Lagrange constraints for transient finite element surface contact". *Int. J. Numer. Methods Eng.,* **32**(1), pp. 103–128. doi : 10.1002/nme.1620320107 - oai: hal-01389918.

[30] Batailly, A., Legrand, M., Millecamps, A., and Garcin, F., 2012. "Numerical-experimental comparison in the simulation of rotor/stator interaction through blade-tip/abradable coating contact". *J. Eng. Gas Turbines Power,* **134**(8), p. 11. doi : 10.1115/1.4006446 - oai: hal-00746632.

[31] Thorin, A., Guérin, N., Legrand, M., Thouverez, F., and Almeida, P., 2018. "Nonsmooth Thermoelastic Simulations of Blade–Casing Contact Interactions". *J. Eng. Gas Turbines Power,* **141**(2), p. 7. doi : 10.1115/1.4040857 - oai: hal-01989188.

[32] Peletan, L., Baguet, S., Torkhani, M., and Jacquet-Richardet, G., 2013. "A comparison of stability computational methods for periodic solution of nonlinear problems with application to rotordynamics". *Nonlinear Dyn.,* **72**(3), pp. 671–682. doi : 10.1007/s11071-012-0744-0 - oai: hal-00813265v1.

[33] Detroux, T., Renson, L., Masset, L., and Kerschen, G., 2015. "The harmonic balance method for bifurcation analysis of large-scale nonlinear mechanical systems". *Comput. Methods Appl. Mech. Eng.,* **296**, pp. 18–38. doi : 10.1016/j.cma.2015.07.017.

[34] Krack, M., and Gross, J., 2019. *Harmonic Balance for Nonlinear Vibration Problems*. Springer, Cham. doi : 10.1007/978-3-030-14023-6.

[35] Xie, L., Baguet, S., Prabel, B., and Dufour, R., 2016. "Numerical tracking of limit points for direct parametric analysis in nonlinear rotordynamics". *J. Vib. Acoust.,* **138**(2), p. 021007. doi : 10.1115/1.4032182 - oai: hal-01265919.

[36] Alcorta, R., Baguet, S., Prabel, B., Piteau, P., and Jacquet-Richardet, G., 2019. "Period doubling bifurcation analysis and isolated sub-harmonic resonances in an oscillator with asymmetric clearances". *Nonlinear Dyn.,* **98**(4), pp. 2939–2960. doi : 10.1007/s11071-019-05245-6 - oai: hal-02295420.

[37] Cardona, A., Lerusse, A., and Géradin, M., 1998. "Fast Fourier nonlinear vibration analysis". *Comput. Mech.,* **22**(2), pp. 128–142. doi : 10.1007/s004660050347.

[38] Jerri, A. J., 1998. *The Gibbs Phenomenon in Fourier Analysis, Splines and Wavelet Approximations*, Vol. 446. Springer, Boston, MA. doi : 10.1007/978-1-4757-2847-7.

[39] Djeddi, R., and Ekici, K., 2016. "Resolution of gibbs phenomenon using a modified pseudo-spectral operator in harmonic balance cfd solvers". *Int. J. Comput. Fluid Dyn.,* **30**(7-10), pp. 495–515. doi : 10.1080/10618562.2016.1242726.

[40] Perret-Liaudet, J., and Rigaud, E., 2006. "Superharmonic resonance of order 2 for an impacting hertzian contact oscillator: Theory and experiments". *J. Comput. Nonlinear Dyn.,* **2**(2), 12, pp. 190–196. doi : 10.1115/1.2447549.

[41] Jiang, H., Chong, A. S. E., Ueda, Y., and Wiercigroch, M., 2017. "Grazing-induced bifurcations in impact oscillators with elastic and rigid constraints". *Int. J. Mech. Sci.,* **127**, pp. 204 – 214. doi : 10.1016/j.ijmecsci.2017.02.001.

[42] Leine, R. I., and van de Wouw, N., 2008. *Stability and Convergence of Mechanical Systems with Unilateral Constraints*. Springer-Verlag Berlin Heidelberg. doi : 10.1007/978-3-540-76975-0.

[43] Bentvelsen, B., and Lazarus, A., 2018. "Modal and stability analysis of structures in periodic elastic states: application to the ziegler column". *Nonlinear Dyn.,* **91**(2), pp. 1349–1370. doi : 10.1007/s11071-017-3949-4 - oai: hal-01686514.

[44] Guillot, L., Lazarus, A., Thomas, O., Vergez, C., and Cochelin, B., 2020. "A purely frequency based floquet-hill formulation for the efficient stability computation of periodic solutions of ordinary differential systems". *J. Comput. Phys.,* **416**, p. 109477. doi : 10.1016/j.jcp.2020.109477 - oai: hal-02864713.

[45] Nayfeh, A. H., and Balachandran, B., 1995. *Applied nonlinear dynamics: analytical, computational and experimental methods*. John Wiley & Sons. doi : 10.1002/9783527617548.

[46] Guckenheimer, J., and Holmes, P., 1983. "Local Bifurcations". In *Nonlinear oscillations, dynamical systems, and bifurcations of vector fields*. Springer, New York, pp. 117–165. doi: 10.1007/978-1-4612-1140-2_3.

[47] Beyn, W.-J., Champneys, A., Doedel, E., Govaerts, W., Kuznetsov, Y. A., and Sandstede, B., 2002. "Chapter 4 - numerical continuation, and computation of normal forms". In *Handbook of Dynamical Systems*, B. Fiedler, ed., Vol. 2 of *Handbook of Dynamical Systems*. Elsevier Science, pp. 149–219. doi : 10.1016/S1874-575X(02)80025-X.

[48] Petrov, E. P., 2016. "Analysis of bifurcations in multiharmonic analysis of nonlinear forced vibrations of gas turbine engine structures with friction and gaps". *J. Eng. Gas Turbines Power,* **138**(10), 04, p. 11. doi: 10.1115/1.4032906.

[49] Seydel, R., 2009. *Practical bifurcation and stability analysis*, Vol. 5. Springer, New York, NY. doi : 10.1007/978-1-4419-1740-9.

[50] Govaerts, W. J. F., 2000. *Numerical Methods for Bifurcations of Dynamical Equilibria*. SIAM. doi : 10.1137/1.9780898719543.

[51] Tisseur, F., and Meerbergen, K., 2001. "The quadratic eigenvalue problem". *SIAM Rev.,* **43**(2), pp. 235–286. doi : 10.1137/S0036144500381988.

[52] Moore, G., 2005. "Floquet theory as a computational tool". *SIAM J. Numer. Anal.,* **42**(6), pp. 2522–2568. doi : 10.1137/S0036142903434175.

[53] Zhou, J., Hagiwara, T., and Araki, M., 2004. "Spectral characteristics and eigenvalues computation of the harmonic state operators in continuous-time periodic systems". *Systems & Control Letters,* **53**(2), pp. 141 – 155. doi : 10.1016/j.sysconle.2004.03.002.

[54] Curtis, C. W., and Deconinck, B., 2010. "On the convergence of Hill's method". *Math. Comp.,* **79**(269), pp. 169–187. doi : 10.1090/S0025-5718-09-02277-7.

[55] Wu, J., Hong, L., and Jiang, J., 2022. "A robust and efficient stability analysis of periodic solutions based on harmonic balance method and Floquet-Hill formulation". *Mech. Syst. Sig. Process.,* **173**, p. 109057. doi : 10.1016/j.ymssp.2022.109057.

[56] Lazarus, A., and Thomas, O., 2010. "A harmonic-based method for computing the stability of periodic solutions of dynamical systems". *Comptes Rendus Mécanique,* **338**(9), pp. 510–517. doi : 10.1016/j.crme.2010.07.020 - oai: hal-01452004v1.

[57] Dou, S., 2022. "An improved tensorial implementation of the incremental harmonic balance method for frequency-domain stability analysis". In Advances in Nonlinear Dynamics, Springer International Publishing, pp. 443–452. doi: 10.1007/978-3-030-81162-4_39.

[58] Kuznetsov, Y. A., 2013. *Elements of applied bifurcation theory*, Vol. 112. Springer-Verlag New York. doi : 10.1007/978-1-4757-3978-7.

[59] Blahoš, J., Vizzaccaro, A., Salles, L., and F., E. H., 2020. "Parallel harmonic balance method for analysis of nonlinear dynamical systems". In Proceedings of the ASME Turbo Expo 2020, p. 12. doi: 10.1115/GT2020-15392.

[60] Ju, R., Fan, W., and Zhu, W. D., 2020. "An efficient Galerkin averaging-incremental harmonic balance method based on the fast fourier transform and tensor contraction". *J. Vib. Acoust.,* **142**(6), pp. 475–498. doi : 10.1115/1.4047235.

[61] Ju, R., Fan, W., and Zhu, W. D., 2021. "An efficient Galerkin averaging-incremental harmonic balance method for nonlinear dynamic analysis of rigid multibody systems governed by differential–algebraic equations". *Nonlinear Dyn.,* **105**, pp. 475–498. doi : 10.1007/s11071-021-06367-6.

[62] Higham, N. J., Mackey, D. S., Tisseur, F., and Garvey, S. D., 2008. "Scaling, sensitivity and stability in the numerical solution of quadratic eigenvalue problems". *Int. J. Numer. Methods Eng.,* **73**(3), pp. 344–360. doi : 10.1002/nme.2076.

[63] Reid, L., and Moore, R. D. Design and overall performance of four highly loaded, high speed inlet stages for an advanced high-pressure-ratio core compressor. Tech. rep., NASA Lewis Research Center Cleveland, OH, United States. url : https://ntrs.nasa.gov/citations/19780025165, 1978 (accessed 2020-10-29).

[64] Piollet, E., Nyssen, F., and Batailly, A., 2019. "Blade/casing rubbing interactions in aircraft engines: Numerical benchmark and design guidelines based on NASA rotor 37". *J. Sound Vib.,* **460**, p. 114878. doi : 10.1016/j.jsv.2019.114878 - oai: hal-02281666.

[65] Colaïtis, Y., and Batailly, A., 2021. "Development of a Harmonic Balance Method-Based Numerical Strategy for Blade-Tip/Casing Interactions: Application to NASA Rotor 37". *J. Eng. Gas Turbines Power,* **143**(11), p. 12. doi: 10.1115/1.4051967 - oai: hal-03286205.

[66] Huebler, D. Rotor 37 and stator 37 assembly. Records of the National Aeronautics and Space Administration, 1903 - 2006. Photographs relating to agency activities, facilities and personnel, 1973 - 2013. https://catalog.archives.gov/id/17468361, 1977 (accessed 2020-10-29).

[67] Woiwode, L., Narayanaa Balaji, N., Kappauf, J., Tubita, F., Guillot, L., Vergez, C., Cochelin, B., Grolet, A., and Krack, M., 2020. "Comparison of two algorithms for harmonic balance and path continuation". *Mech. Syst. Sig. Process.,* **136**, p. 106503. doi : 10.1016/j.ymssp.2019.106503 - oai: hal-02424746.

[68] Cameron, T. M., and Griffin, J. H., 1989. "An alternating frequency/time domain method for calculating the steady-state response of nonlinear dynamic systems". *J. Appl. Mech.,* **56**(1), pp. 149–154. doi : 10.1115/1.3176036 - oai: hal-01333697.

[69] Sarrouy, E., and Sinou, J.-J., 2011. "Non-linear periodic and quasi-periodic vibrations in mechanical systems - on the use of the harmonic balance methods". In *Advances in Vibration Analysis Research*, F. Ebrahimi, ed. IntechOpen, Rijeka, ch. 21, pp. 419–434. doi : 10.5772/15638 - oai: hal-00730895.